Universidad Carlos III de Madrid

Bachelor Thesis

Aerospace Engineering

Unsteady loads on an airfoil during the deployment of a flap

Author:
Enrique
Hernández-Hurtado
Esquilas

Thesis Advisor:
Manuel
García-Villalba
Navaridas

Spring 2014

Para mi tío Juanjo

Agradecimientos:

Me gustaría expresar mi agradecimiento muy especialmente hacia Manolo y Óscar por haberme dado la oportunidad de coaborar con el Departamento, y por su ayuda y continuo interés desde el principio. También quisiera acordarme de forma muy afectuosa de Manu por los buenos ratos que hemos pasado. Agradecerle el haberme ayudado tanto con todo, y felicitarle por el gran trabajo que está realizando. Quisiera acordarme también de todo el resto del Departamento de Ingeniería Aeroespacial, y Biomédica. No he parado de aprender y me habéis hecho sentir muy a gusto. Me alegro mucho de compartir estos meses con todos. También acordarme de mi familia por su apoyo constante. Y los más importantes, los que no pueden estar con nosotros.

Abstract

The effect of suddenly deflecting a trailing-edge flap on an airfoil is studied using a validated, two-dimensional Navier-Stokes code which utilizes the Immersed-Boundary Method. The flight regime for the airfoil lies in the ultra-low Reynolds number range (Re $\sim$ 1000). The angle of deflection approaches a step function to simulate the sudden deflection of the flap. The effects of varying both the flap-angle amplitude and the speed of deflection are also investigated. A model is developed using the obtained data in order to predict the lift response for any flap-angle evolution. The model is in agreement with the simulation data.

Bachelor Thesis

Universidad Carlos III de Madrid

Unsteady loads on an airfoil during the deployment of a flap

Enrique Hernández-Hurtado Esquilas

Thesis Advisor: *Manuel García-Villalba Navaridas*

Contents

List of Figures

1 Introduction

1.1 Motivation

Since the Wright brothers first flight in 1903, the general tendency in aviation has been to develop vehicles which are both bigger and faster. No matter how good was the performance of a flying machine, or which consequences would need to be taken; if men were able to fly a bigger aircraft, or to do it faster, aeronautical engineering was going in the right direction.

When analysing the aerodynamic forces, a parameter of importance is the so-called Reynolds number. It is defined as $\mathrm{Re} = \frac{\rho U_\infty c}{\mu} = \frac{U_\infty c}{\nu}$ (where ρ is the fluid density, U_∞ is the free-stream velocity, c is the length of the airfoil chord, μ is the fluid dynamic viscosity and ν is the kinematic viscosity of the fluid). As planes have grown bigger and faster, this leads to a quasi-exponential growth in the Reynolds number with the years.

In fact, the variation of the Reynolds number throughout history for several iconic aircraft is shown in Figure 1, in logarithmic scale.

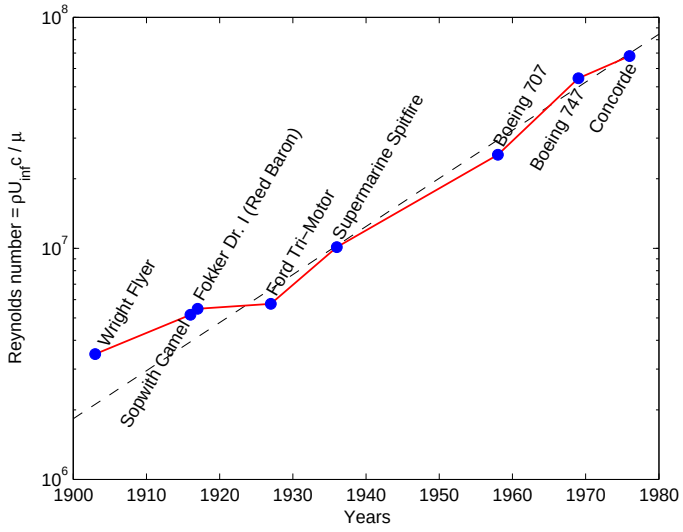

Figure 1: Variation of the Reynolds number throughout history (logarithmic scale).

The Reynolds number for aircraft is seen to increase its value as the time goes

by, in an exponential fashion (linear in logarithmic scale, as shown by the green curve fitting).

However, there is an interesting fact when studying nature, and it is that flying animals perform their flights in a low-Reynolds-number regime, which of course is not the case for human-made flying machines. This leads to the question of how good can the performance be in this regime, and how this could be applicable for aircraft, as, for instance, in the creation and development of Micro Air Vehicles (MAVs).

MAVs are aeroplanes with a maximum size of 15 cm, and can serve for both academic and research purposes. But there is also a huge amount of possible applications for them, ranging from photography, scouting for rescue missions or in catastrophic events such as nuclear accidents, as well as helping control crowds of people, and they are also to be used for military purposes.

MAVs are a promising field of research for the future. It is true that there have been regulatory issues concerning their use in recent times. There has been some controversy related to the use of MAVs in the civil air space. More generally, UAVs (Unmanned Aerial Vehicles) of any size flying in the civil territory have been a reason of argument due to the possibility of them colliding against airliners [1]. Because of this, the United States' Federal Aviation Administration (FAA) needs to set regulations to the use of UAVs [2]. The effects to be analysed by this study are not in the field of this flight rules, so it is free from the cited regulatory issues.

These MAVs make use of profiles and features which needs to be optimized for this low-Reynolds number regime, in contrast with the general tendency of aviation to produce machines operating at high Reynolds-numbers. Because of these differences, the design and development of MAVs is not at the same technological point at which conventional aeroplanes are placed. This is partly because in the MAVs flight conditions there appear unsteady aerodynamics phenomena that are still not efficiently predicted and controlled [3]. These phenomena include the so-called leading-edge vortex (LEV), which appears on the airfoil leading-edge as the flow separates and further reattaches before reaching the airfoil trailing-edge. This effect is seen for instance in insect flight and is an example of the peculiarities of the unsteady, low-Reynolds number flow [3].

When designing a MAV, it is important to select the proper airfoil for its wing and also to be able to have a proper control mechanism. A flap gives the ability to

control the airfoil forces and moments, and so its motion, making it manoeuvrable and useful for flight. In the present study, this part is the main focus of interest. Making use of a Navier-Stokes solver, the force response when suddenly deflecting a flap in a low-Reynolds number airfoil is to be investigated. This code uses an immersed-boundary method, and will be also described in the present thesis.

1.2 State of the art

Although the effect of flap deflection on the airfoil aerodynamic forces has already been studied, there are still many issues that need to be understood about it. In fact, when it comes to the rapid, unsteady flap deflection, there are not many studies performed, and the range of Reynolds numbers for the analysis done is usually high ($\mathrm{Re} \sim 10^6$).

Besides, most of the papers are directly focused on obtaining a control mechanism for the airfoil. In [4], they try to make use of this feature in order to alleviate the unsteady loading produced in wind turbine blades due to atmospheric turbulence. A rapidly-deflected, trailing-edge flap is used and actively controlled. The study is performed using a high-order panel model, validated with experimental data coming from a water tunnel. The study is mainly focused on computing the constants of the PID controller.

More interesting studies to support the study in hand relate directly to the aerodynamic effect of the flap deflection, on an already-oscillating airfoil [5–9].

What is mainly done is to deflect the flap harmonically, with a frequency independent from that of the airfoil motion [5, 6, 9]. Several deflection parameters (ramp rate, start time, ...) are taken into account.

One interesting feature is that the process of LEV formation and shedding processes are not influenced by the flap deployment [5, 7]. However, the pressure on the LEV (and so the loading) is indeed affected by the starting time of the flap deployment [5], and the control flap deflection can reduce slightly the strength of the LEV [7].

It is also possible to analyse the combined effect of both the angle of flap deflection and the angle of attack (α) on either the lift or the pitching-moment coefficient, defined respectively as $C_l = \frac{L}{\frac{1}{2}\rho U_\infty^2 c}$ and $C_m = \frac{M_y}{\frac{1}{2}\rho U_\infty^2 c^2}$, where L is the airfoil lift force, M_y is the moment about the y-axis (pitching moment), ρ is the

fluid density, U_∞ is the free-stream velocity and c is the airfoil chord. This is done by plotting superimposed functions of both angles [6]. The main effect is seen in the maximum value of the lift coefficient, which increases when both angles increase at the same time. The opposite happens when both decrease.

Other study [7] makes use of PIV for the analysis. It is observed that an upward flap deflection reduces the maximum negative pitching moment and the maximum lift coefficient due to the lower-surface suction pressure.

The downward flap deflection induces a positive-camber effect that increases the maximum value of the lift coefficient ($C_{l_{max}}$) and the pitch-down peak pitching moment ($C_{m_{peak}}$). The LEV detachment occurs when the airfoil pitches down [7].

Some other studies focus their attention on the flap effect on the pitching moment for the oscillating airfoil [8]. In [8], the study is performed on a tunnel facility, and the flap deflection is done in three stages: deployment, steady-state phase and closing. The steady-state phase is added because it is seen to be beneficial for controlling the moment.

Several effects are observed: reducing the maximum negative pitching moment is best done by using a fast deployment rate and a start time near the mean angle (rapid deflection). Nevertheless, this also leads to a decrease in the maximum (peak) lift coefficient. The best compromise is an upward flap deflection a bit after the mean angle (during pitch-up), remaining steady for a short period and then returning to its initial position [8].

The effect of the flap deflection on the wing-tip vortex has also been studied [9].

The vortex displacement is more effective for downward deflections, and the highest rates lead to the biggest vortex displacements. Negative flap deflections are seen to move the vortex outboard, strengthen it, and increase its size [9].

Besides analysing flap deflections, spoilers have also been already studied in [10]. An in-house code is used; it develops a two-step numerical method (Gauss-Seidel) to solve the Navier-Stokes equations. The grid system is a chimera made up of two different areas: a fixed mesh for the airfoil, and a moving grid for the spoiler, selecting the overlapping points by means of a dynamic domain-dividing line (DDDL) [10].

The change in lift due to the sudden spoiler deflection has three stages:

1. An initial decrease (undershoot), which can be observed at the highest deployment rates, due to the suction bubble appearing just downstream of the

spoiler and the pressure increase upstream of it because of the rapid, dynamic spoiler deployment.

2. A lift increase when the suction bubble effect is cancelled by the pressure build-up upstream of the spoiler. This generates a lift overshoot, in which a peak is reached when the reattachment point of the separation bubble just touches the trailing edge.

3. A lift decrease following the bubble burst, and setting the lift to a mean value (convergence) smaller to the initial one.

The peak in the second stage is seen to increase when the deployment rate increase, up to a certain value in which it starts decreasing instead.

But not only experimental or simulated studies have been carried out. Indicial concepts have also been used to study aerodynamic flap effects in [11], where the model is presented and validated using comparisons with experimental data.

1.3 Objectives

The goals to be achieved during the present study are listed below:

1. To determine the optimum resolution of the simulation domain in terms of grid points. This would be the value to be used in the simulations of the study.

2. To obtain the temporal response, in terms of aerodynamic forces, to a sudden trailing-edge flap deflection on an airfoil. The response is unsteady, and we seek to find the rapid force evolution as a response to the flap deflection. We will focus on the unsteady-response part, and not on the steady-state convergence. For this, several cases are to be defined, and they are to be run using the code for the study.

3. To be able to vary the parameters defining the flap-angle evolution, and to study their effect on the aerodynamic forces. This way it is possible to change the amplitude and speed of deflection, and to analyse how the force response is influenced by them.

4. To be capable of visualizing the flow and understanding the different phenomena behind the force variation. This way it will be possible to explain the force variation in terms of either pressure or velocity contours on the fluid domain.

5. To create an approximated model to predict the force evolution. The model is to be based on the results for some of the flap deflections, and it will be able to give a prediction for the forces when the flap parameters are changed.

Although the force response to the flap deflection is the main focus of the present study, it is not the only feature to be investigated, but only the second part of a bigger project. It is desired to create an efficient MAV in the future, and for this there is a process to be followed. The first step is to make an analysis in search of the best airfoil to operate in the low-Reynolds number flight regime. The present study is the second part of the process, in which a flap is added to the airfoil in order to get an insight into how the forces vary with the sudden flap deflection. This would make it possible to control the MAV in a proper way in the future.

The airfoil-selection process has also been considered and analysed. Potential methods have been chosen for it, and the best airfoil has been chosen in terms of the maximum aerodynamic efficiency. However, because the present thesis is focused on the effect of the flap deflection, the airfoil characterization study is presented apart in full in Appendix B. The flap analysis is presented below.

2 Methodology

2.1 Software

The main tool to be used is a Computational-Fluid-Dynamics (CFD) code. This code has been developed by Manuel Moriche [13] in the Aerospace Engineering Department at Carlos III University.

2.1.1 The Navier-Stokes solver

The core of the code is an algorithm to solve the Navier-Stokes equations in two-dimensional form on a rectangular domain. It is a direct-numerical-simulation (DNS) code, so that the Navier-Stokes equations are solved directly, needing no model to simulate the turbulent effects. The code to be used is two-dimensional. This is because we are to simulate an airfoil, assumed to be the cross-section of an infinitely-long wing. This implies the assumption that the flow is fully two-dimensional, which is true as long as the Reynolds number is low enough. As the Reynolds number for the study lies in the ultra-low range, we are going to have accurate results without needing extra modelling for any three-dimensional effect.

The Navier-Stokes equations for a viscous, incompressible, Newtonian fluid with constant properties, read (in non-dimensional form) [13]:

$$\frac{\partial \vec{u}}{\partial t} + (\vec{u} \cdot \nabla)\vec{u} = -\nabla p + \frac{1}{\mathrm{Re}}\nabla^2 \vec{u} \tag{1a}$$

$$\nabla \cdot \vec{u} = 0 \tag{1b}$$

Here, $\vec{u}$ is the non-dimensional fluid velocity, t is the non-dimensional time and p is the non-dimensional pressure. $\mathrm{Re} = \frac{U_\infty c}{\nu}$ is the Reynolds number, which is the only parameter on Equation 1.

The domain of simulation must be rectangular and uniformly meshed. The domain limits are termed x_0 and x_f respectively as the lower and upper limits in the x-direction, and y_0 and y_f respectively as lower and upper limits in the y-direction.

The code makes use of a *staggered* grid. This means that the horizontal and vertical velocities, and the pressure, are not all computed on the same points. An

illustration of the staggered grid in shown in Figure 2. The longitudinal velocity, u, is computed at the locations represented by an horizontal arrow ($\rightarrow$), the vertical velocity, v, is found in the points marked by a vertical arrow ($\uparrow$), and the pressure, p, is obtained where the dots are placed ($\bullet$).

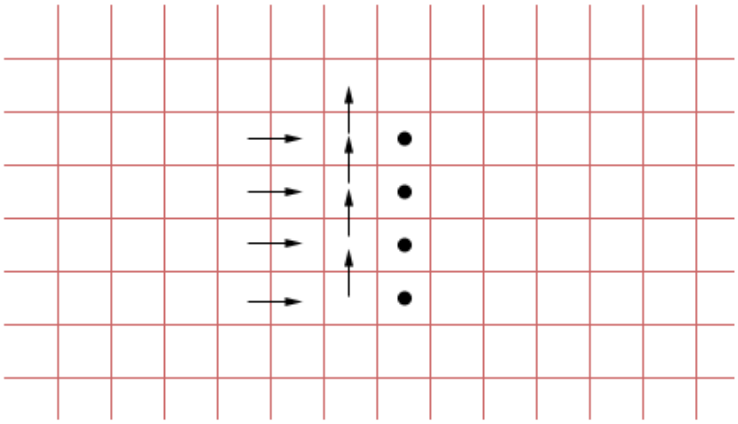

Figure 2: The staggered grid used in the computations.

The number of points in the x-direction is termed n_x, and that in the y-direction is named n_y. The mesh-width in x- and y-directions is therefore given by Equation 2.

$$\Delta x = \frac{x_f - x_0}{n_x} \tag{2a}$$

$$\Delta y = \frac{y_f - y_0}{n_y} \tag{2b}$$

The boundary conditions to be used by the code are illustrated in Figure 3. It is to be noted that the code allows to have an outflow boundary condition in the east boundary. This is done by using an advective condition which gives exit to the flow pattern without affecting the solution inside the domain.

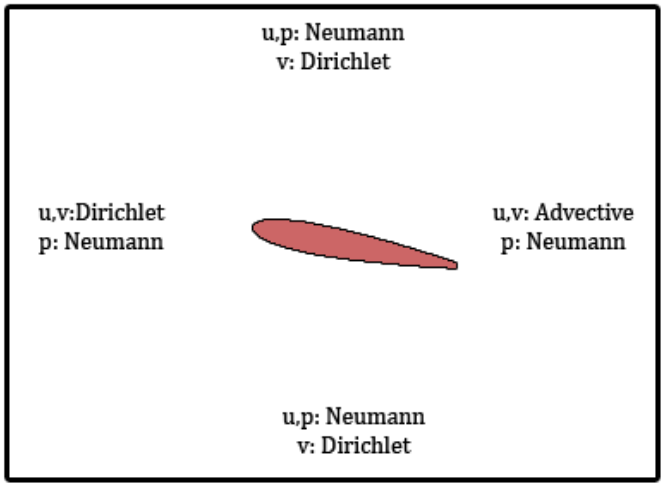

Figure 3: Boundary conditions for the domain.

2.1.2 The Immersed-Boundary Method

The presence of the body (in our case, the airfoil) in the flow is introduced by means of an Immersed-Boundary Method (IBM) [13].

The body is rigid. The IBM is computationally efficient at low Reynolds numbers, specially for moving bodies. This makes the IBM more preferable for the problem in hand than body-fitted grid methods.

We set two different domains: the Eulerian (fluid), fixed, and the Lagrangian (body) moving. In [12] the presence of the solid body is substituted by a forcing term ($\vec{f}$) added to the momentum equation. This becomes:

$$\frac{\partial \vec{u}}{\partial t} + (\vec{u} \cdot \nabla)\vec{u} = -\nabla p + \frac{1}{\mathrm{Re}}\nabla^2 \vec{u} + \vec{f} \tag{3}$$

The forcing term, $\vec{f}$ is added in order to fix the velocity at the boundary of the body to have the non-slip condition. It is computed as follows [12]:

1. Estimate explicitly the velocity in the Eulerian frame.

2. Interpolate this estimated value to the Lagrangian grid.

3. Compute the needed volume force from the desired velocity and that estimated at the Lagrangian grid.

4. Take this volume force from the Lagrangian to the Eulerian domain.

2.1.3 Code validation

The full code has been subjected to a process of validation using both analytical solutions and more advanced simulations. The full validation methods can be found in [13]. The results showed good agreement and the code has been thus validated.

2.1.4 Parallelization

The code has been developed to simulate both two- and three-dimensional flows. Due to the fact that 3D simulations are very resource-consuming, using a serial code is not recommended. Therefore, the code has been optimized to be used in parallel as explained in [13]. This will also make possible to use the hardware tools to be described in Section 2.2.

2.2 Hardware

The main hardware tool to be used is a computational cluster on Carlos III University. It allows not only a parallel computation but a distributed one. Parallel computation, or multiprocessing (MP) is done in such a way that several process can be running in different processors, but all placed on the same computer machine. Distributed computing, referred to as Message Passing Interface (MPI), allows having several computers interconnected, each of which may also have several processors working.

The main advantage of having distributed computing is that it allows having different machines instead of needing a single computer with many processors. The price of adding processors to the same computer grows exponentially and becomes unaffordable from a certain point on. The drawback is that a very fast bus is needed to communicate externally among machines.

The cluster used for the present work makes use of distributed computing. It has 13 nodes, each one having 12 processors for computation. One of the 13 nodes

is termed the *master*. Its function is to keep the essential services for the parallel-computation system, such as holding the current configuration, allowing for node installation, being used as the login node to access the cluster system, etc. The other nodes have only installed the computational software needed for calculus.

The different nodes are connected to each other through a high-speed bus of the *Infiniband* type. Connexion to the master node is done using the normal network, and this fast bus is used for communication among nodes when parallel computing is already taking place inside the cluster.

Another feature of the cluster (due to the fact that it makes use of distributed computing) is that it presents a queuing system. This is also managed by the master node. The queuing manager allows sending tasks to the cluster even when no processors are available. These tasks are placed into a sort of waiting list and they will be executed when the sufficient number of processors is available. This allows maximizing the system efficiency by reducing the idle time to a minimum.

3 Computational set-up

3.1 Finding the optimum resolution

Having accurate results has a cost both in terms of computer and time. In principle, the higher the resolution, the higher the accuracy, but also the higher the cost. However, this is true up to a point, in which the increase in accuracy starts to be negligible while the cost keeps on increasing.

For the current study, an analysis was carried out to assess the effect of the grid resolution on the results, in order to be able to select the best value for it.

For this to be done, the flow around an NACA 0006 (at zero angle of attack) was chosen as an example. The Reynolds number for the analysis is Re = 1000. The time-step is $\Delta t = 0.0024$, such that the CFL is always lower than 0.6 [14, 15]. Several resolution values were to be analysed, and the domain of analysis was set fixed for all of them (the domain is $[x_0, x_f] \times [y_0, y_f] = [-6, 10.3840] \times [-8.1920, 8.1920]$; see Figure 4).

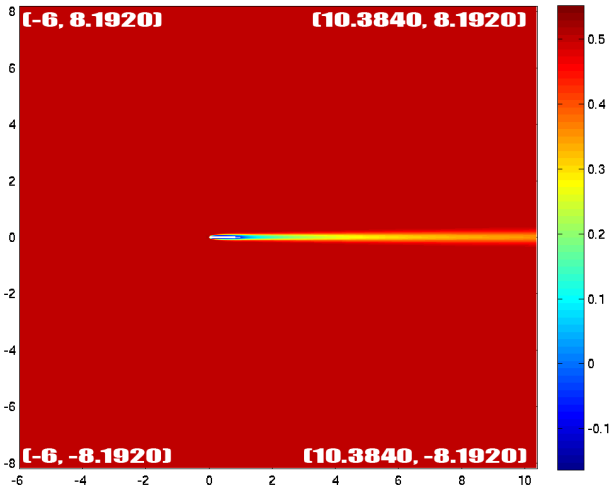

Figure 4: Coordinates of the domain for the resolution cases (Units normalized with the airfoil chord).

The values for the resolution were measured in grid points, being the four analysed: $n_x \times n_y = 1024 \times 1024$, $n_x \times n_y = 2048 \times 2048$, $n_x \times n_y = 4096 \times 4096$

and $n_x \times n_y = 8192 \times 8192$. n_x and n_y are, respectively, the number of grid points in x- and y-directions, as defined in Section 2.1.

The highest-resolution case ($n_x \times n_y = 8192 \times 8192$) is chosen to be the reference solution for the problem, and the other cases are to be compared against it.

This is done in two different ways:

1. By comparing the aerodynamic forces (lift and drag) on the airfoil.

2. By comparing the velocity profiles along the airfoil surface.

The results are shown below.

3.1.1 Aerodynamic forces

The lift and drag coefficients are defined as $C_l = \frac{L}{\frac{1}{2}\rho U_\infty^2 c}$ and $C_d = \frac{D}{\frac{1}{2}\rho U_\infty^2 c}$, where L is the airfoil lift force, D is the drag, ρ is the fluid density, U_∞ is the free-stream velocity and c is the airfoil chord. Both C_l and C_d are found for each of the cases, and compared to the correct values. The obtained coefficients are shown in Table 1, where *error* is referred to the 8192×8192 case. The lift coefficient given by the potential theory is $C_l = 0$ for $\alpha = 0$. Thus the differences in the lift coefficient are assumed to be negligible in all cases, and the relative errors are not shown.

Resolution	C_l	Error	C_d	Error
1024×1024	3.6234×10^{-6}	-	0.1101	2.419%
2048×2048	1.0517×10^{-7}	-	0.1082	0.6512%
4096×4096	-9.7426×10^{-8}	-	0.1077	0.186%
8192×8192	7.5573×10^{-7}	-	0.1075	0%

Table 1: Resolution results for NACA 0006.

Due to the fact that the airfoil is very thin, the same study was proposed to be carried out for an NACA 0012, again at $\alpha = 0$. This way the effect of thickness could be assessed and taken out of the equation. The results for the NACA 0012 are presented in Table 2. Again, the errors on C_l are not taken into account since it is considered to be $C_l = 0$ in all cases as predicted by the theory.

Resolution	C_l	Error	C_d	Error
1024×1024	-3.40094×10^{-7}	-	0.1240	2.564%
2048×2048	7.1142×10^{-7}	-	0.1217	0.662%
4096×4096	-7.7875×10^{-8}	-	0.1211	0.165%
8192×8192	1.0720×10^{-8}	-	0.1209	0%

Table 2: Resolution results for NACA 0012.

Besides, the results of the relative differences on the drag coefficients are represented graphically in Figure 5 for both airfoils.

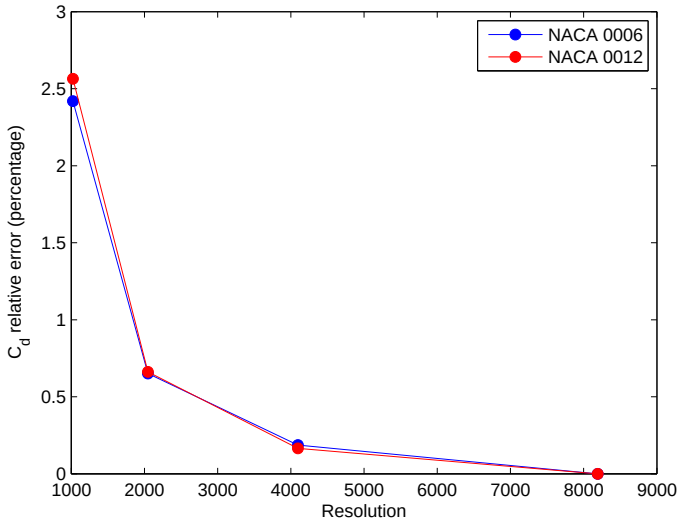

Figure 5: The relative error of the lift and drag coefficients with respect to the 8192×8192 case.

The effect of thickness is seen to be negligible, as expected, as both lines lie on the same one. According to the aerodynamic forces, 2048×2048 already gives a relative error smaller than 1% which is considered to be acceptable.

3.1.2 Velocity profiles

The second figure of merit is the profile of velocity along a line normal to the airfoil surface, as shown in Figure 6. In this picture, the normal lines have been placed

on $\frac{x}{c} = \{\eta_t, \frac{1}{2}\eta_t, \frac{1}{2}, \frac{3}{4}\}$. η_t is defined as $\eta_t = \frac{x_{t_{max}}}{c}$, being $x_{t_{max}}$ the x-coordinate of the point of maximum thickness. For both NACA 0006 and NACA 0012, $\eta_t \approx 0.3$.

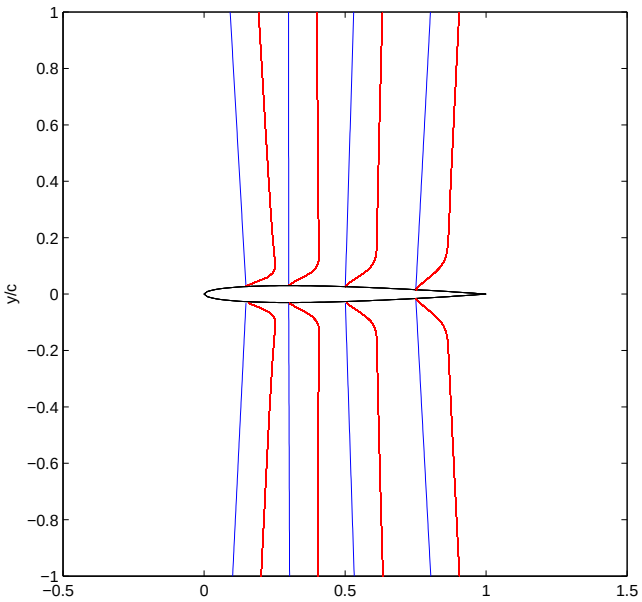

Figure 6: The velocity profiles on a set of normals to the surface (NACA 0006).

Figure 7 shows the velocity profile on a line tangent to the airfoil surface at the point of maximum thickness, i.e., $\eta_t = 0.3$. Focusing on one of the profiles (see Figure 7), the results are seen to match those given by the aerodynamic forces: the relative difference starts being negligible from 2048×2048 on.

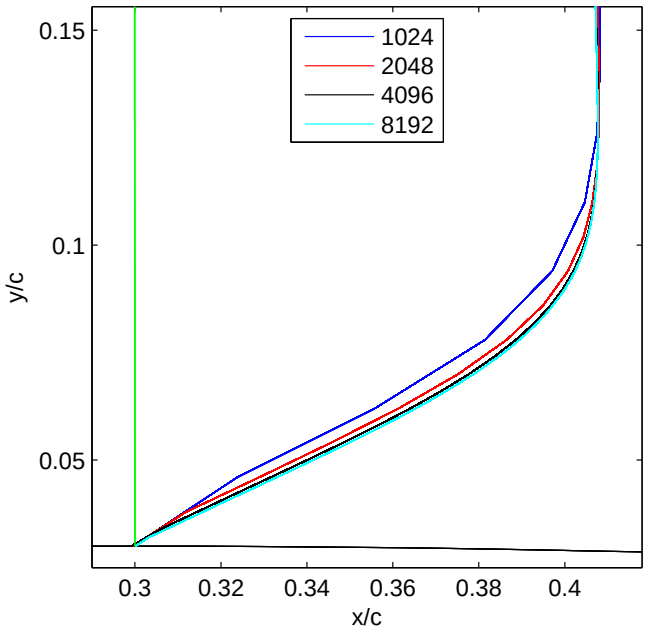

Figure 7: Velocity profiles for the different resolutions (NACA 0006).

Again, the process is also done for an NACA 0012, as shown in Figure 8. The location of the normal line is the same as in Figure 7. The results also match those given before.

3.1.3 Conclusions

When studying a resolution problem, one would like to have the minimum loss of accuracy with the minimum possible cost. According to the results given before, this is accomplished by the lowest resolution whose relative error is considered negligible, i.e., 2048×2048.

Taking the domain in hand, it is possible to compute the grid spacing, leading to $dx = dy = 0.0080$, which indeed gives a value of 125 points per chord.

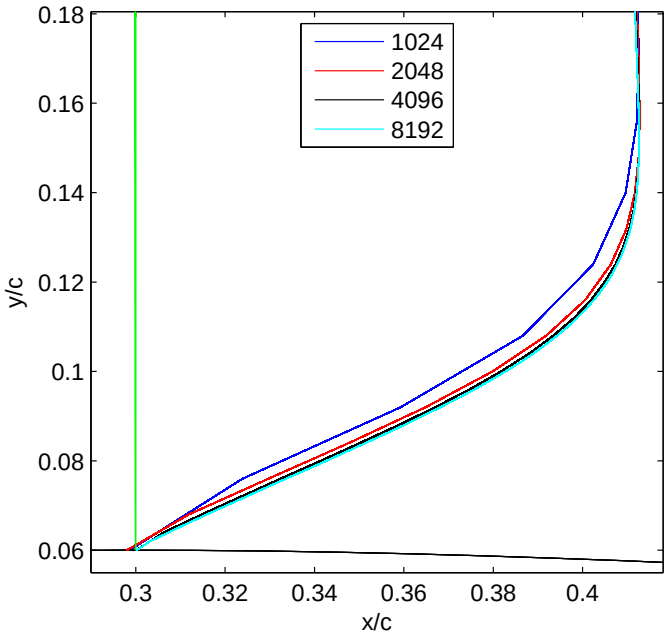

Figure 8: Velocity profiles for the different resolutions (NACA 0012).

3.2 Flap-deflection evolution

After having established the optimum grid resolution in the previous section, it is time to continue with the study on the sudden flap deflection. The next step in the analysis is to define a function that describes the temporal evolution of the flap angle.

This will be described as:

$$\theta(t) = \frac{1}{2}A(\tanh(\tau) + 1), \tag{4}$$

where A is the maximum deflection angle (in radians) and the time coefficient, τ, is defined as

$$\tau = m(t - t_{off}). \tag{5}$$

Here, t stands for non-dimensional time, such that $t = \frac{\text{time}}{t_c}$, where the characteristic time, t_c represents the time needed for a fluid particle to cross the airfoil chord, i.e. $t_c = \frac{c}{U_\infty}$. m is a measure of the maximum curve slope (maximum

rotary speed, in rad), and t_{off} (also made non-dimensional with t_c) is the time instant where this maximum slope takes place. It is to be noted that m is actually the slope (in $\frac{rad}{s}$) multiplied by t_c so as to maintain consistency with the unit convention. These parameters are illustrated in Figure 9.

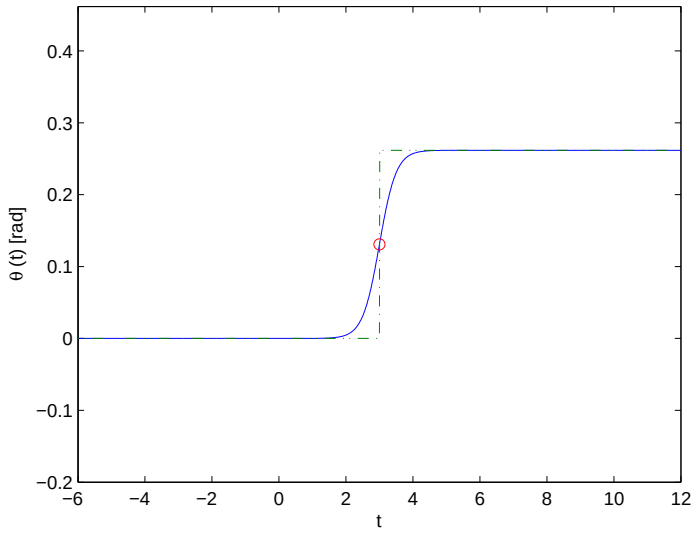

Figure 9: An example of the flap deflection-angle evolution as a function of time (blue line), alongside the step function (green dashed line). $A = 15$ deg $= 0.2618$ rad, $m = 2$ rad, $t_{off} = 3$

This flap deflection has been chosen due to its similarity to the step function (as it can be seen in Figure 9), which is made smooth this way in order to approach real effects, and to better be able to tune it, by changing the parameters (A, m and t_{off}) defining it. The flap is deflected counter-clockwise.

3.3 Geometry

The airfoil to be analysed will be a flat plate with zero thickness. This way neither camber nor thickness effects will alter the solution. As a future task, it is proposed to add these two effects, and to study how they influence the results from the present study.

Although the airfoil to be analysed has ideally zero thickness, in the simulation it will have a thickness of the order of Δx. This is because, in order to have the

non-slip condition, the code assigns a value of the volume force to the Lagrangian points of the body, which makes the thickness to vary with the grid resolution. This effect has not been analysed and it is left as a future task to study the airfoil thickness for the simulations.

The flap-hinge is to be placed at a point 75% after the airfoil trailing-edge. For all the cases of study, the angle of attack of the profile is $\alpha = 0$ deg.

3.4 Base case

After having shown the previous steps, it is now time to define the parameters corresponding to the case of study. The Reynolds number lies in the ultra-low range, being Re = 1000 (defined by the airfoil chord and the fluid properties). The time step is $\Delta t = 0.0024$. It has been chosen so that the CFL [14, 15] for the simulation is always lower than 0.6.

The domain of analysis is defined such that an approximate length of five chords lie ahead of the airfoil, ten after it, and five both above and below the profile. This means that the domain is $[x_0, x_f] \times [y_0, y_f] = [-5, 9.976] \times [-4.992, 4.992]$, being the airfoil leading edge placed at the origin. The grid is made such that the 125-points-per-chord rule (see Section 3.1) is met ($dx = 0.0080$). This means $n_x = 1872$ and $n_y = 1248$.

With these parameters, the base case is run, which will be used as a base for the different cases to be run later on.

The obtained lift coefficient is $C_l = 0$, as predicted by the theory for a flat airfoil with no angle of attack [16]. The drag coefficient reads $C_d = 0.1013$.

3.5 Cases of study

The next step is to define the cases to be studied. There are two main sets of parameters whose effect is to be studied:

1. The maximum deflection angle, represented by the amplitude, A.
2. The deflection speed, given by both the maximum slope (m) and the time offset (t_{off}).

Cases	1	2	3	4	5	6	7
A (deg)	5	7.5	10	12.5	15	17.5	20

Table 3: Amplitude cases.

There are seven different values of the amplitude to be analysed, as presented in Table 3. The speed is represented by five different cases, illustrated in Table 4. Here, t_{action} is the time required for the flap to be fully deflected.

Cases	A	B	C	D	E
m (rad)	0.5	1	2	5	10
t_{off}	10	6	3	2	0.5
t_{action}	10	5	2	1	0.5

Table 4: Speed cases.

These cases are to be combined in such a way that both amplitude and speed effects are studied, as it will be presented in Section 4. All cases have Re $= 10^3$ and the same domain and grid-points distribution described in Section 3.4.

4 Results

In this section, the results of the analyses are presented.

4.1 Effect of amplitude

The first effect to be analysed is that of the maximum flap-deflection amplitude. For this purpose, the deploying speed is set fixed for all of the cases at a value such that $m = 2$ rad, and $t_{off} = 3$. The deflection-angle amplitude correspond to those given in Table 3. The angle evolution is shown in Figure 10 for these cases.

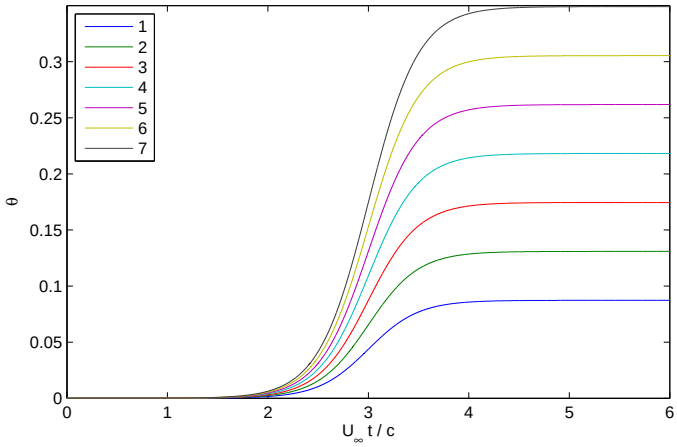

Figure 10: The angle evolution for the amplitude cases shown in Table 3.

The results are first shown in Figure 11 for the lift-coefficient evolution.

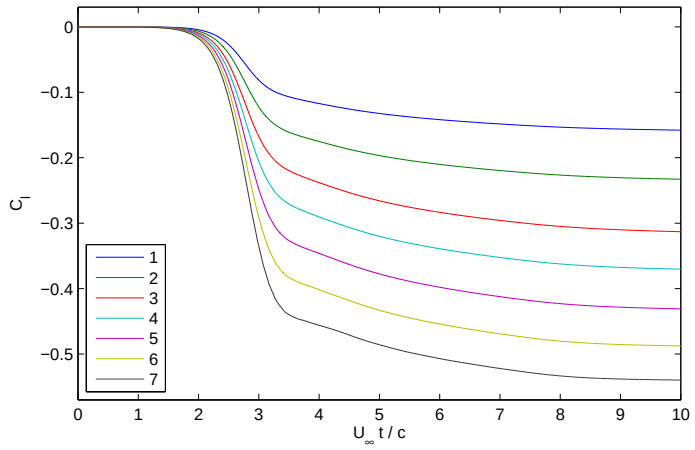

Figure 11: The airfoil lift-coefficient evolution depending on the maximum deployment amplitude, as a function of time.

As it can be extracted from Figure 11, the main effect of an increase in the flap-angle amplitude is to increase the value of $C_{l_{max}}$. This resembles an increase in the airfoil camber, given by the flap deployment.

Figure 12 shows the drag-coefficient variation for the different amplitude cases.

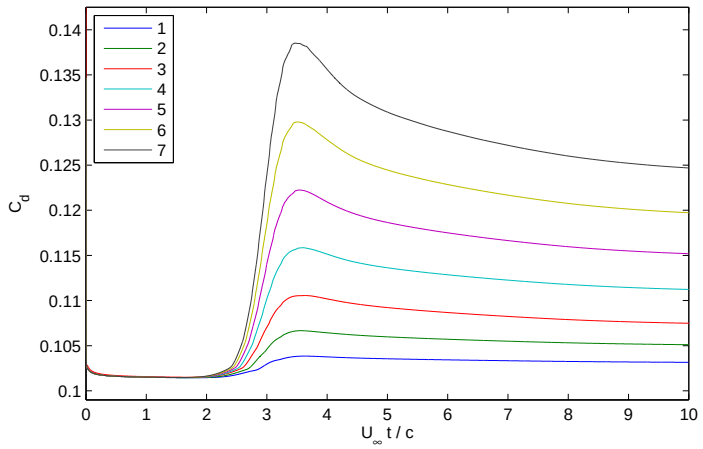

Figure 12: The effect of the flap maximum amplitude on the drag-coefficient response.

The drag too increases as the amplitude does so. This is due to the change in geometry and also to the increase in the induced drag.

No oscillations appear on either of the force responses for the analysed cases, and the transient response follows the same pattern. This is due to the fact that all cases follow the same deployment rate and evolution, and these conditions will change when the deflection speed varies, as it will be shown in Section 4.2.

4.2 Effect of speed

The effect of the deployment rate is next investigated. For this, the amplitude is set fixed at a value of $A = 10$ deg for all cases, while the speed parameters are varied according to the cases in Table 4. These evolution of angles is depicted in Figure 13.

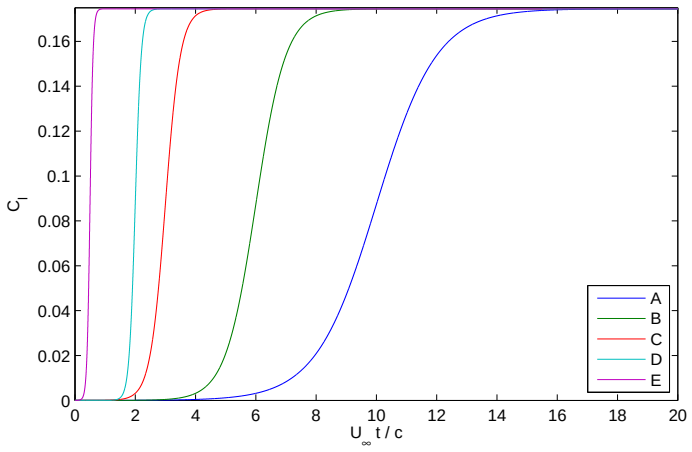

Figure 13: The angle evolution for the slope cases shown in Table 4.

Because of the differences in deflection speed, it was proposed to use a different value of the time step (Δt) for each of the cases. This could be achieved by using an adaptive Δt which would increase as the speed of deflection is reduced. This was thought to be done in order to have more accuracy for the fastest cases, while not wasting resources on the slower ones.

However, a curious result was seen as not all the cases converged to the same value of either C_l or C_d (see Figure 14). This is not a correct result, because, as the amplitude is set fixed for all the cases, the final state should be the same for all.

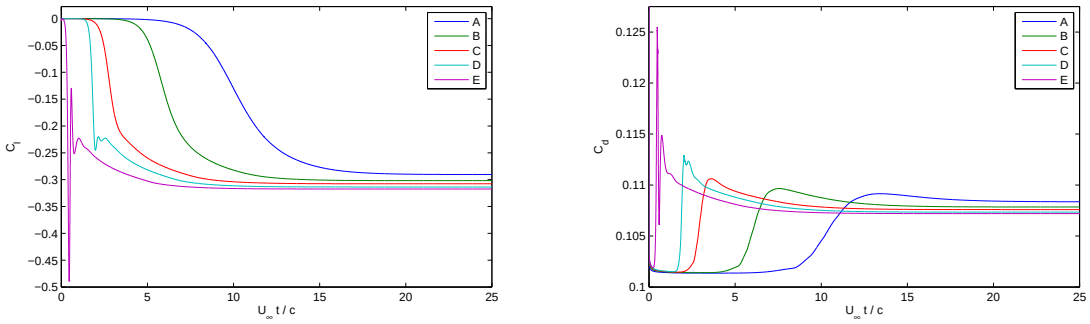

(a) C_l (b) C_d

Figure 14: Non-convergent results for adaptive values of Δt.

The explanation for this lies in the fact that the code has a numerical error which is proportional to both ν and Δt. Therefore, the higher Δt the higher the error. Because there is also a dependence on ν, if the Reynolds number were to be lowered, the time step should be, too. For the problem in hand, the difference in $C_{l_{end}}$ was eliminated by setting the same Δt for all of the cases. This was the Δt of the fastest case (Δt_{min}), in order to have the highest accuracy.

Figure 15 shows the lift-coefficient evolution following flap deployment at several rates. The first thing to note is that there is a critical value of the deployment rate beyond which there start to appear oscillations in the force evolution. This value corresponds to just above that of case C ($m = 2$ rad).

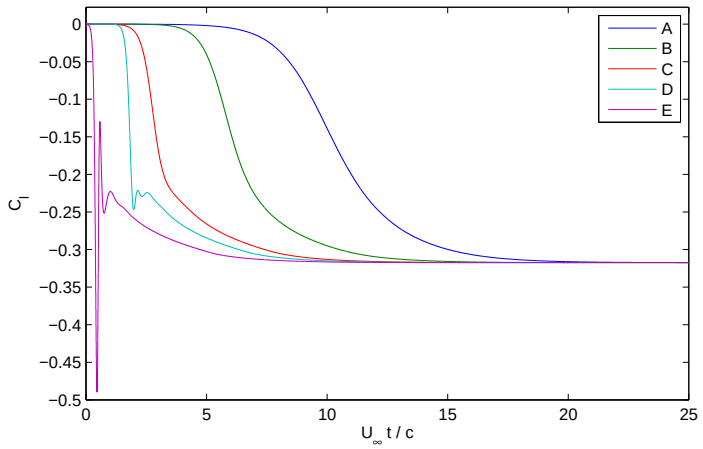

Figure 15: The effect of the deploying rate on the lift coefficient (as a function of the non-dimensional time, $\frac{U_\infty t}{c}$).

For the cases below this critical speed, the response is smooth and follows the evolution of the deflection angle. This is because the deflection time is such that it takes more time for the flap to be deflected than for a fluid particle to travel the whole airfoil chord (i.e., $t_{action} > 1$). However, as the deployment time starts reaching a value of unity, the flap speed becomes critical and there starts to be vortex shedding which produces oscillations on the force.

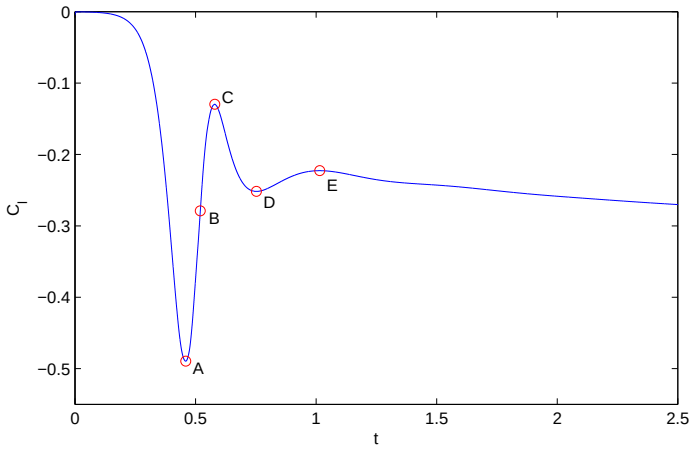

Figure 16: The lift response for the fastest case (speed case E).

Another fact is that the faster the deployment, the bigger the oscillation peak-

values. The lift coefficient of the fastest case (case E) is shown again in Figure 16 with more detail. Figure 17 shows the pressure contours at the different points marked in Figure 16. The temporal evolution for the cases of $t_{action} \lesssim 1$ follows the following pattern:

1. An initial increase in the lift absolute value (overshoot) due to the flap sudden deflection which resembles a negative camber. There is a sudden increase in the pressure just upstream of the flap, and a suction bubble is created downstream of it. It is this suction bubble that makes the airfoil to be subjected to a negative lift. When the pressure on the bubble reaches a minimum (point A), the C_l is minimum, too.

2. Then the effect of the suction bubble is shaded by the pressure increase ahead of the flap. This makes the lift's absolute value to decrease. A bubble is being formed on the flap tip (this is illustrated point B). When this bubble just leaves the airfoil trailing-edge, the absolute value of the lift reaches a minimum (point C).

3. There is finally an increase in the lift absolute value as the bubble is separated from the airfoil and shed downstream (point D). There is a small increase in lift absolute value when the flap is slowed-down until it is fully-deployed (point E).

4. Once the flap has been completely deflected, the lift smoothly converges to its steady-state value.

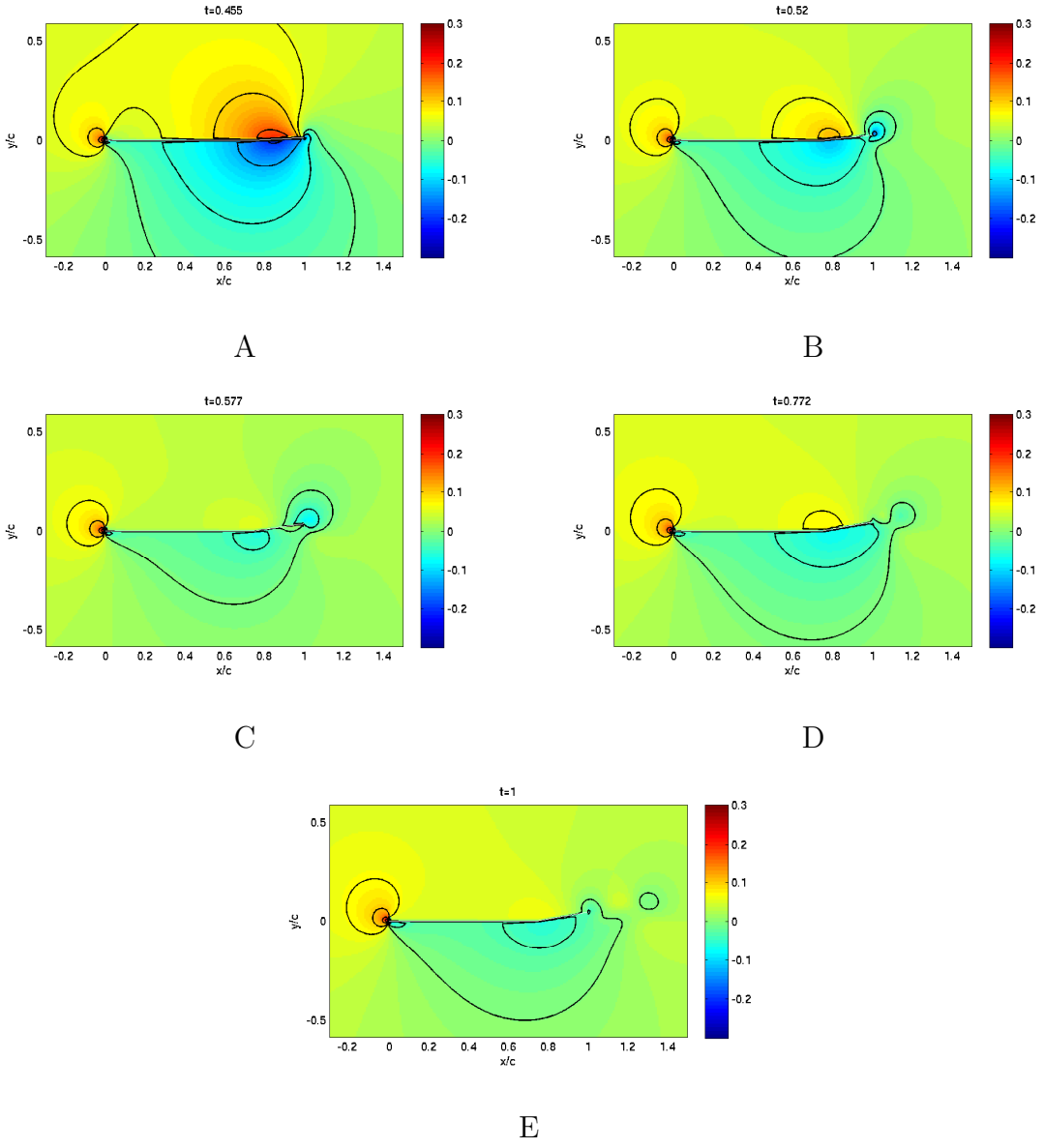

Figure 17: Instantaneous pressure contours for the time instants marked in Figure 16. The airfoil is drawn in white colour.

It is also noticeable the fact that no matter the deployment rate all cases converge to a value of the lift coefficient (Figure 15), and that this value is the same for all of them. This is because of the fact that all cases have the same value

of the deployment amplitude, A, and the same time step (Δt).

It is also possible to depict the vorticity contours for this case E. The result is shown in Figure 18. Note that the pictures have been zoomed out to better appreciate the vortex shedding. The time instants have been selected in steps of 0.5 time units from $t = 0.5$.

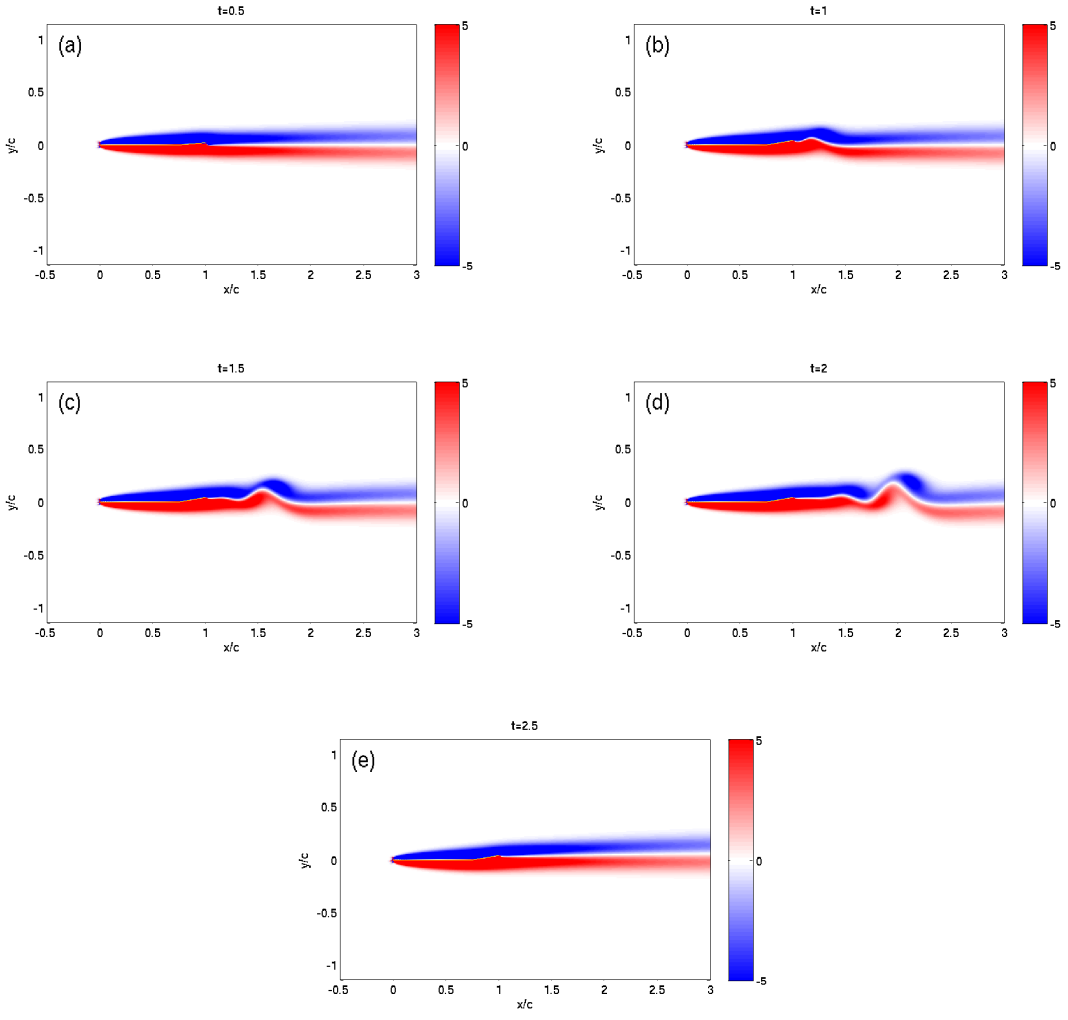

Figure 18: Contours of vorticity for different time instants ($A = 10$ deg).

Figure 18 reveals a disturbance on the wake. In order to better visualize the vortex being shed away from the profile, it was proposed to analyse the same case

E, but reaching a higher angle of flap deflection. The parameters defining this new case are $A = 20$ deg $= 0.3491$ rad, $m = 10$ rad, $t_{off} = 0.5$. Its vorticity contours are shown in Figure 19. The time instants are the same as for Figure 18.

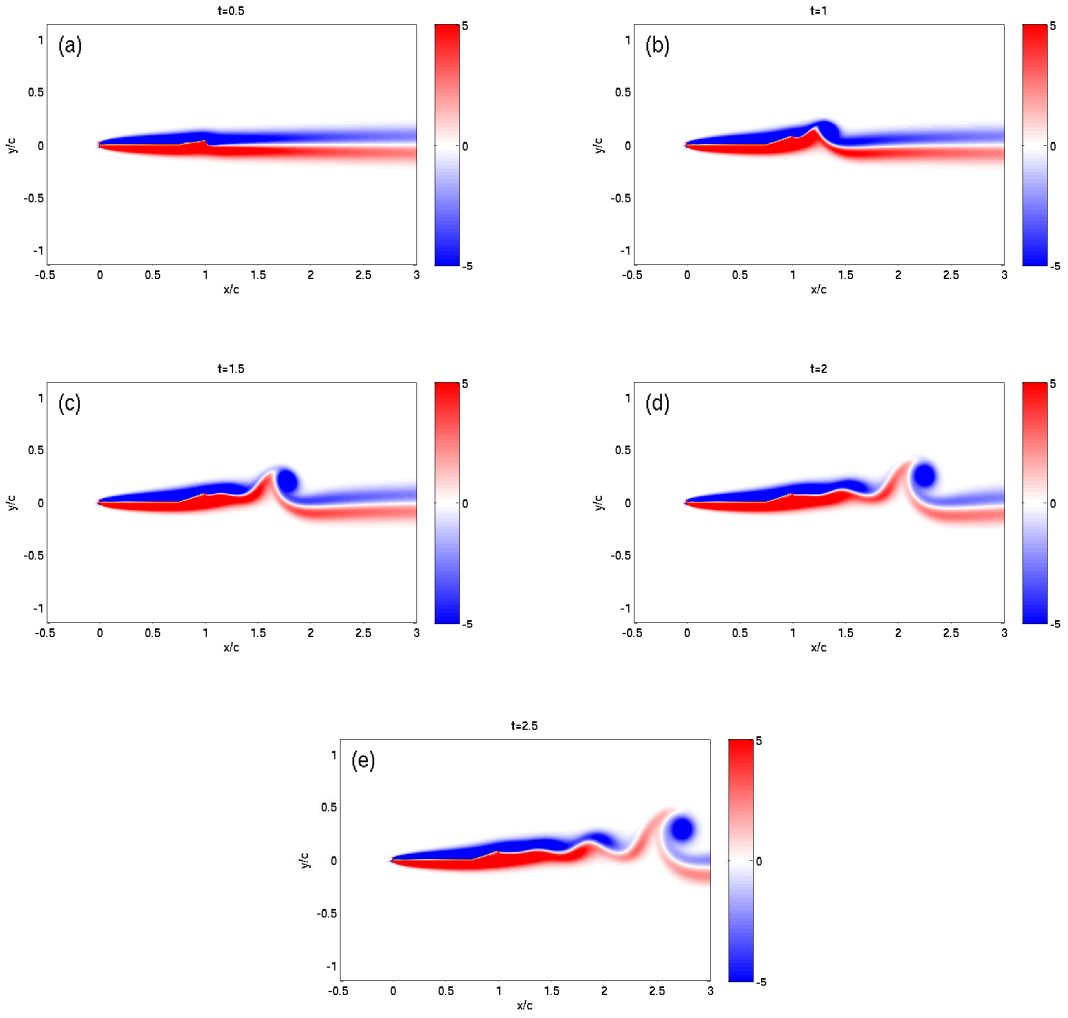

Figure 19: Contours of vorticity for the time instants in Figure 18, for a case of $A = 20$ deg.

In Figure 19, it is possible to better visualize how the vortex shedding process indeed takes place. The higher value of the maximum amplitude makes it easier to be visualized.

The response of the slowest case (case A) is seen to be smooth (Figure 15) and to follow approximately the shape of its deflection angle. It was seen that no vortex-shedding process took place. This was done by contouring its vorticity at times ranging from $t = 0.05$ to $t = 0.25$, in steps of 0.05. The result is shown in Figure 20, where no vortex shedding is appreciated.

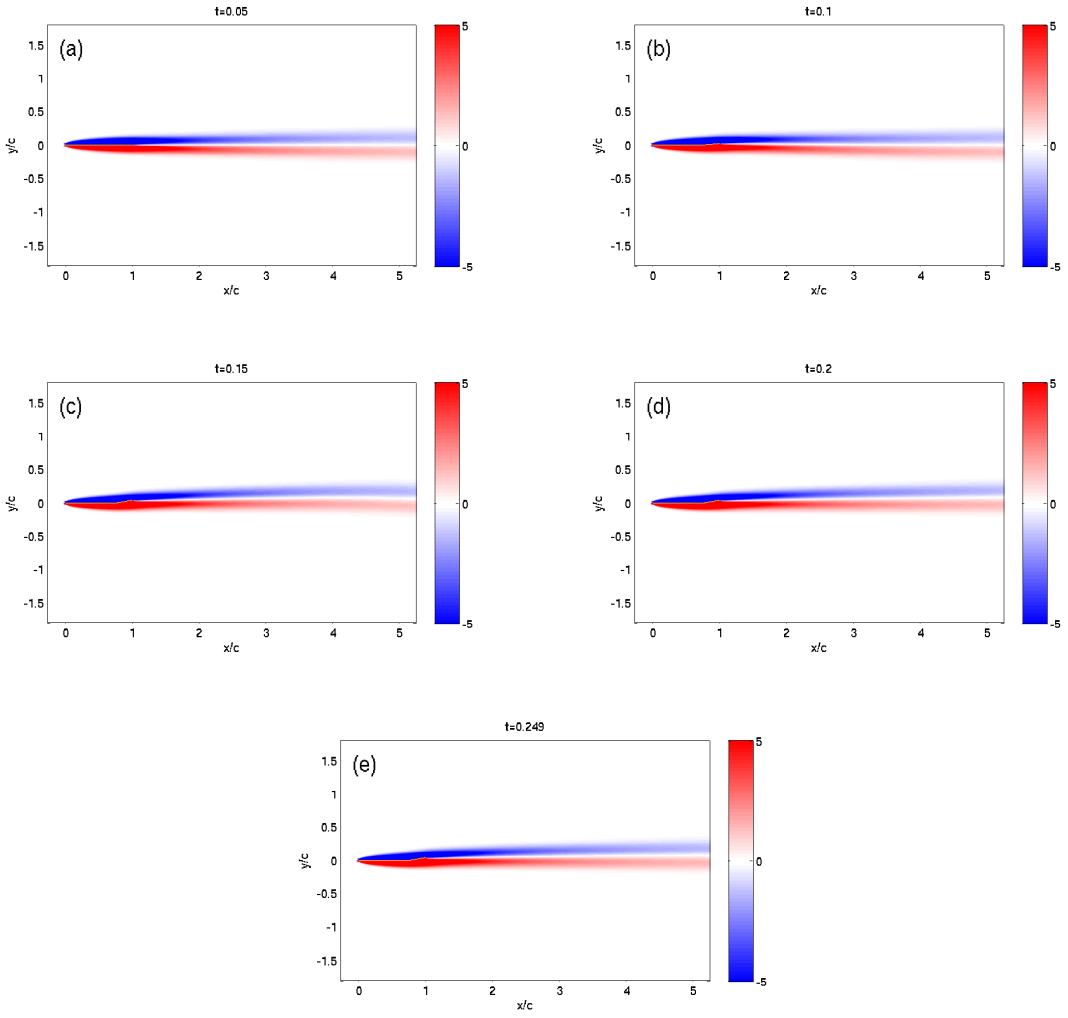

Figure 20: Contours of vorticity for slowest case.

As a result, it was to be checked whether it was possible to have vortex shedding at that lowest speed. For this, the same case was analysed, but this time up to

an amplitude of $A = 40$ deg. The other parameters were set equal to case A. The vorticity contours are shown in Figure 21.

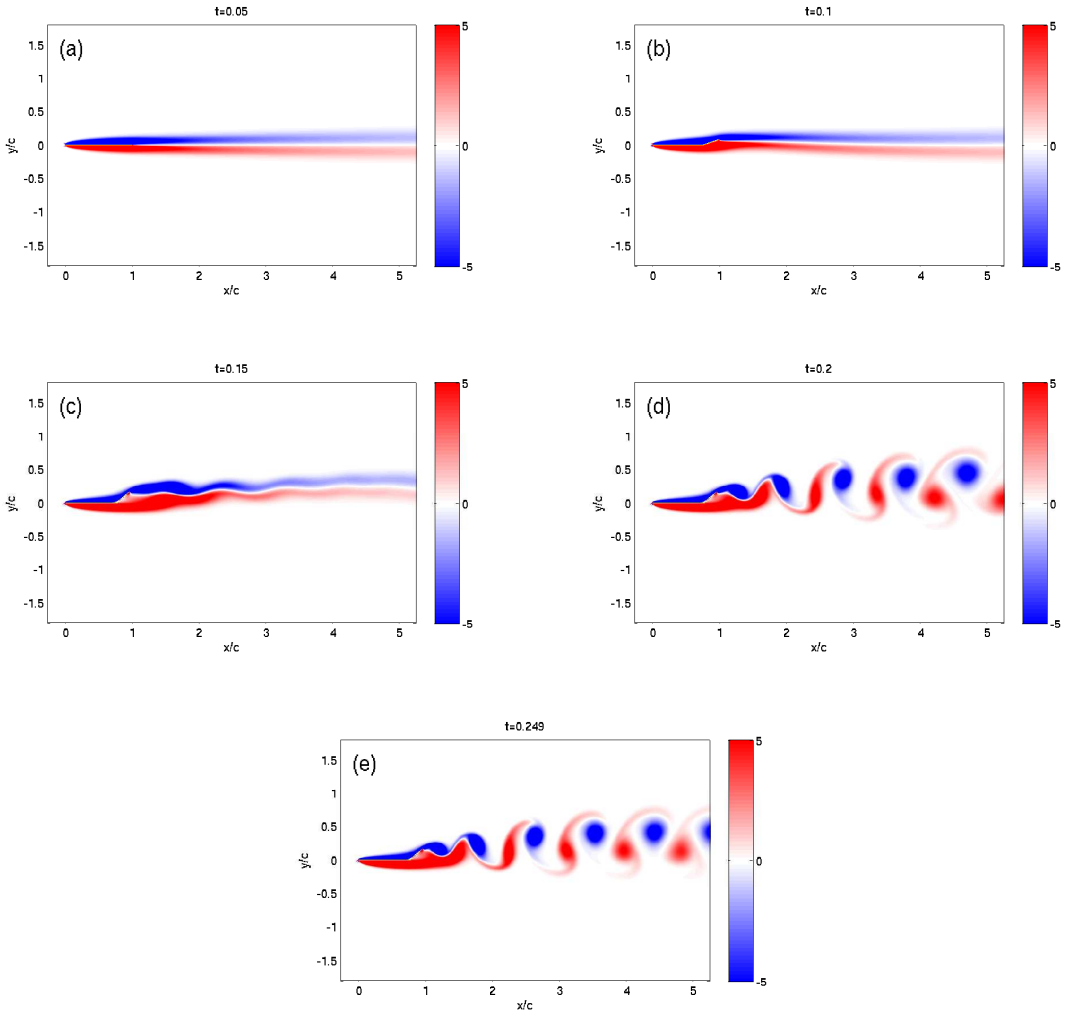

Figure 21: Contours of vorticity for the slowest case up to an amplitude of $A = 40$ deg.

Figure 21 proves that it is possible to have vortex shedding even in the slowest-deployment conditions. In fact, there is a Karman vortex-street appearing in the flow, which makes the aerodynamic forces to oscillate as shown in Figure 22.

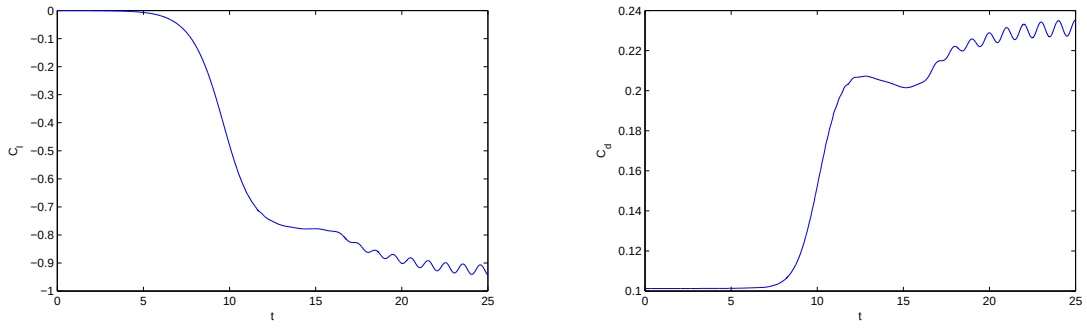

(a) $C_l\ (t)$ (b) $C_d\ (t)$

Figure 22: Evolution of aerodynamic forces for the slowest case when $A = 40$ deg.

Figure 23 shows the response on the drag coefficient. Again, for $t_{action} \lesssim 1$ the pressure fluctuations make the force evolution to oscillate before reaching the steady-state value. This happens in the same manner as for the lift coefficient, as it was illustrated in Figure 15.

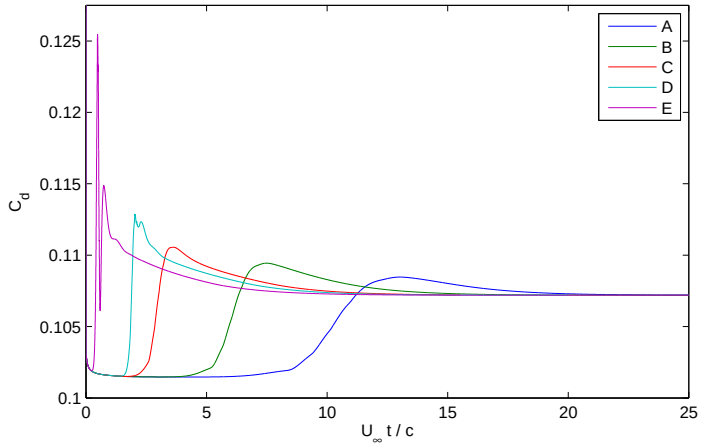

Figure 23: The deployment-rate effect on the drag coefficient (versus non-dimensional time).

It is also possible to plot the force responses as a function of the time parameter, τ. This is the best way to visualize how the speed variations influence the solution when they all respond to the same deflection-angle evolution. This is shown in

Figure 24

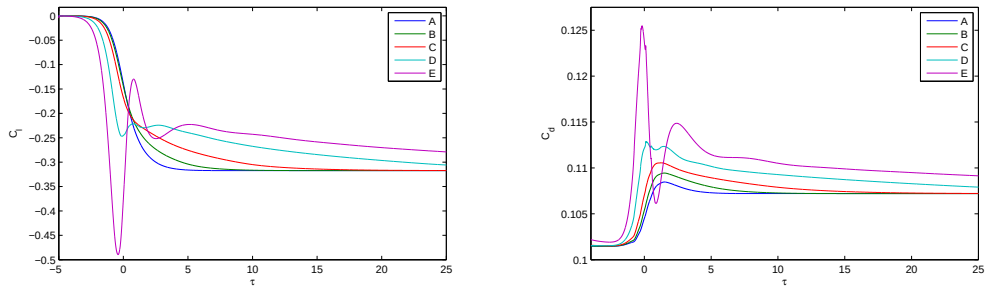

(a) C_l (τ) (b) C_d (τ)

Figure 24: The effect of the flap deployment rate on the force response (as a function of the time parameter, τ).

4.3 Model development

The next step in the present study is the development of a simple model to predict the force response for a given flap-angle evolution. The idea of this model is to make use of a convolution function, obtained from one of the cases, in such a way that it is able to give the force evolution for any other case.

When referring to a sudden change in angle of attack, the Wagner function is frequently used. The Wagner function is a measure of how the lift coefficient (ΔC_l) varies when suddenly varying the angle of attack ($\Delta\alpha$) [17]. It is usually taken by its approximate value, given in [18]. This reads:

$$\phi_w(s) = 1.0 - 0.165e^{-0.0455s} - 0.335e^{-0.3s} \tag{6}$$

where $\phi_w(s)$ is the Wagner function, being s the distance travelled in semi-chords by a fluid particle from the leading-edge. Figure 25 illustrates Equation 6.

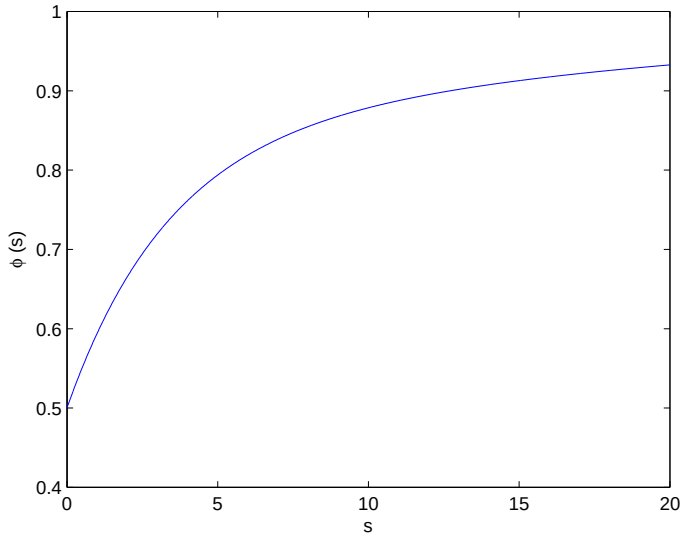

Figure 25: The Wagner function given by its approximation.

The first idea for the modelling process was to directly convolve this Wagner function with the angle evolutions in order to predict the lift coefficient. However the results were not satisfactory. It is important to remember that the Wagner function is derived in the high-Reynolds number regime, where viscous effects'

importance is lowered. As the Reynolds number is decreased (as it happens for the ultra-low range of the present study), viscosity effects cannot be disregarded. Besides, the Wagner function is done for a sudden change in the airfoil angle of attack, while what we are modifying here is the angle of the flap.

For these reasons, it was proposed to create a model in which to use new function, ϕ, in order to predict the force evolution instead of the Wagner function.

The model is to be used only for the lift coefficient. In the present study, no accurate results have been obtained for the drag as this is much more influenced by shape, separation or turbulence features. It is left as a future task to produce a similar model for this horizontal force.

4.3.1 General formulation

In the first approximation, the function to compute the lift coefficient is modelled as the sum of two different functions, as follows:

$$C_l(t) = F_1(t) + F_2(t), \tag{7}$$

where $F_1(t)$ is referred to the unsteady response, and $F_2(t)$ represents the slowly convergent, steady-state part.

In order to gain accuracy when representing all the different cases, a weight parameter is to be added to Equation 7. This way, this equation really becomes

$$C_l(t) = \gamma F_1(t) + (1-\gamma)F_2(t), \tag{8}$$

where γ is the weight parameter, being $\gamma = 0$ a fully-unsteady approximation and $\gamma = 1$ a steady-state result. Tuning the value of γ will help model all the different reactions.

Now it is time to define the functions F_1 and F_2. Since F_2 is referred to the steady state, it will be a function of the flap-angle time evolution, $\theta(t)$, so that for long times the results depends only on θ_{max}, being θ_{max} the maximum, end value of the flap angle deflection. Therefore, F_2 is actually $F_2(t, \theta(t))$. It will be modelled as

$$F_2(t) = \xi\theta(t). \tag{9}$$

Since for long times the only dependence is on $\theta(t)$, ξ is chosen to be constant, so that the response is directly proportional to $\theta(t)$.

The function F_1 is referred to the unsteady evolution. Thus, instead of being directly influenced by $\theta(t)$, it must be a function of its first time-derivative, named as $\dot{\theta}(t)$. Besides, it is at this point where we must make use of the convolution function to define F_1 as

$$F_1(t) = \int_0^t \phi(t-\tau)\dot{\theta}(\tau)\,\mathrm{d}\tau. \tag{10}$$

In here, $\phi(t)$ is no longer a constant, but a time-dependent function. It is to be convolved with the angle first time-derivative in such a way that the unsteady response is predicted.

In the end, the function to model the airfoil lift coefficient is

$$C_l(t) = \gamma \int_0^t \phi(t-\tau)\dot{\theta}(\tau)\,\mathrm{d}\tau + (1-\gamma)\xi\theta(t) \tag{11}$$

4.3.2 Parameter determination

It is now time to define all $\phi(t)$, ξ, and γ.

Since $\phi(t)$ makes reference to the unsteady part, it is part of the convolution integral. The fastest case (case E) is to be assumed to represent a step function (to be used in the convolution). Therefore, $\phi(t)$ is to be coming from this fastest case. In particular,

$$\phi(t) = \begin{cases} 0 & \text{if } t \leq 0 \\ \frac{C_{l_{fastest}}(t)}{\theta_{max}} & \text{if } t > 0 \end{cases}. \tag{12}$$

When determining ξ, it is important to remember that this part of the equation refers to the steady state. Thus, the information is to be extracted from the slowest case, i.e., case A. We define ξ as

$$\xi = \frac{C_{l_{slowest}}}{\theta(t)}. \tag{13}$$

Once all the other parameters have been obtained, it is time to define the weight parameter, γ. This parameter represents the weight given to either the unsteady response or the steady-state convergence. This means that, in the two extreme

cases, $\gamma = 0$ would represent a non-oscillatory, slow response, while $\gamma > 0$ would introduce oscillations, and in the extreme $\gamma = 1$ represents a fully non-stationary, fast response.

This means that γ is a free-to-tune parameter, which can be adjusted to improve the accuracy of the model. Thus, it is supposed to have a different value of γ depending upon the case that is to be modelled. Therefore, instead of directly selecting a value for γ, the results will be presented for both of the extreme cases, $\gamma = 0$ and $\gamma = 1$, for each of the cases.

4.3.3 Results

As stated before, the results have been obtained for C_l for all the cases, having both extreme cases $\gamma = 0$ and $\gamma = 1$. These are shown in Figures 26 and 27.

The cases have been divided into *slow* ($t_{action} > 1$) and *fast* ($t_{action} \lesssim 1$). The slow cases are shown in Figure 26 and the fast ones, in Figure 27.

What Figure 26 tells us is that, for ($t_{action} > 1$), the fully-steady-state approximation ($\gamma = 0$) is accurate for short times. This is because the evolution of the flap deflection is smooth for short times, as it was shown in Figure 13. Therefore, a quasi-steady approximation is enough to predict the lift coefficient. However, as the flap-deflection speed increases, there start to appear unsteady-aerodynamics phenomena. This is why both curves do not match from the point of maximum slope on (for $\gamma = 0$).

It is at this point that the unsteady approximation starts to approach the real value of the lift coefficient. As the flap is rapidly deflected, the aerodynamics of the problem become non-stationary and the unsteady approximation fits better. After the flap is fully deflected, there may appear vortex shedding (as discussed before). This is why the final state is well predicted by the unsteady approximation.

The same happens for the fast cases (Figure 27). Besides, in these cases the unsteady model introduces a source of oscillations, which gives more accurate results. Again, the $\gamma = 0$ cases are give better results for short times, while the long-time response is better predicted by the unsteady ($\gamma = 1$) model.

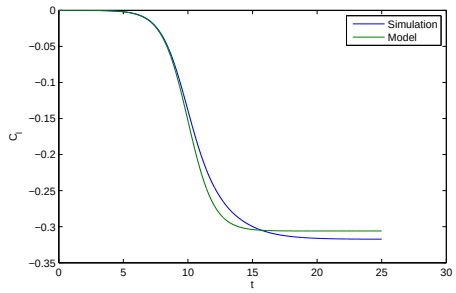

(a) Case A, $\gamma = 0$

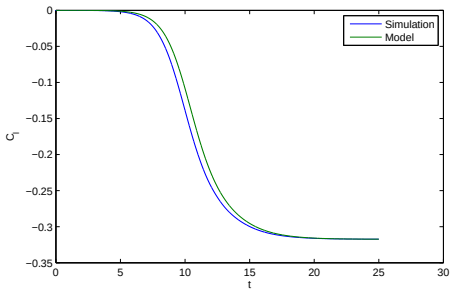

(b) Case A, $\gamma = 1$

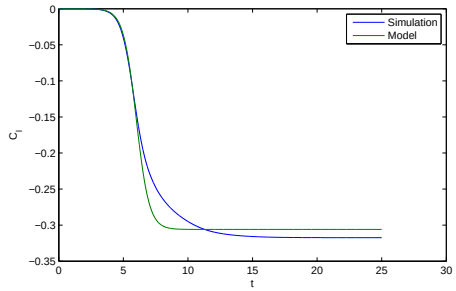

(c) Case B, $\gamma = 0$

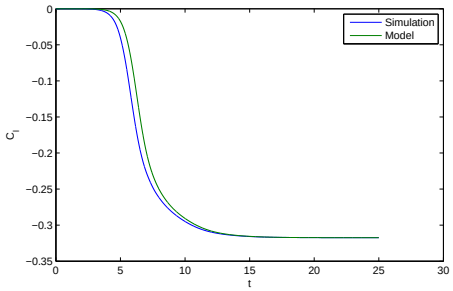

(d) Case B, $\gamma = 1$

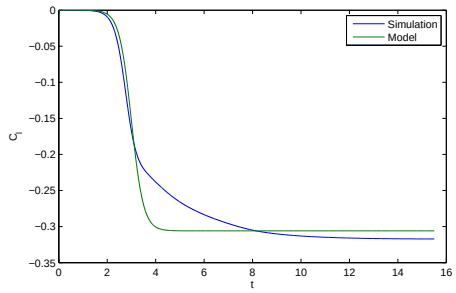

(e) Case C, $\gamma = 0$

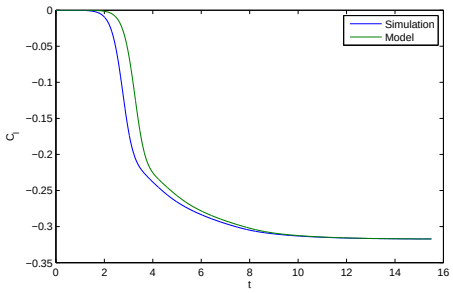

(f) Case C, $\gamma = 1$

Figure 26: Model results for the different cases and for the two extreme values of γ. *(1), slowest cases.*

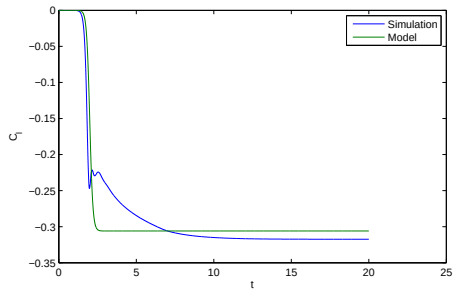

(*g*) Case D, $\gamma = 0$

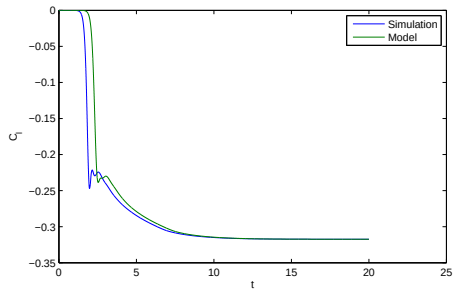

(*h*) Case D, $\gamma = 1$

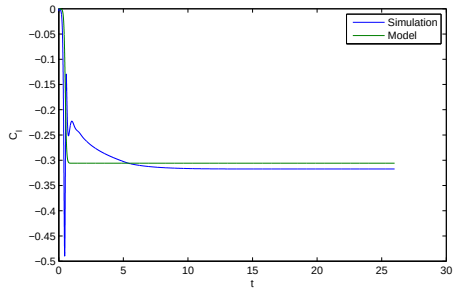

(*h*) Case E, $\gamma = 0$

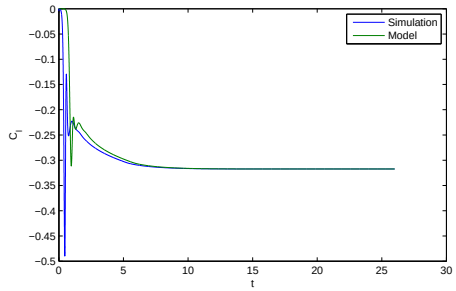

(*i*) Case E, $\gamma = 1$

Figure 27: Model results for the different cases and for the two extreme values of γ. *(2), fastest cases.*

5 Conclusions

5.1 Summary

In the present study, it has been investigated the effect of suddenly deflecting a flap on a flat airfoil with no thickness. The flap was placed on the airfoil trailing-edge, and the analysis has been carried out in terms of aerodynamic forces. A Navier-Stokes-solver code has been utilized, which makes use of an Immersed-Boundary Method to simulate the presence of the body into the flow. The focus of attention has been the unsteady response, as the flap is assumed to be deflected in an abrupt fashion.

It has been possible to assess the effect of both amplitude and speed of the flap deflection. Increasing the amplitude only increases the value of $C_{l_{max}}$ and C_d. However, as only the amplitude was varied, and for this the speed was fixed constant, no changes were introduced into the unsteady response.

Increasing the speed of flap deflection has, however, an influence on the unsteady response. It has been tested by setting a fixed amplitude. Therefore, the steady-state value has been the same for all speed cases, either on the lift or on the drag coefficient. There has been identified a critical case from which on the response is no longer smooth but oscillations are present. This happens for $t_{action} \lesssim 1$, being t_{action} the time needed to fully-deflect the flap. Because the time is made non-dimensional with $\frac{c}{U_\infty}$, this means that unsteadiness becomes critical when the time needed to deflect the flap is of the order of (or lower than) that needed for a fluid particle to cross the airfoil chord.

Analysing pressure contours on the airfoil, it has been possible to explain the oscillatory behaviour of the force response. Vorticity contours has also been obtained, and it has been proved that a vortex-shedding process indeed takes place on the airfoil.

Finally, a model has been developed in order to predict the force evolution for different flap deflections. This model is separated into two main parts: one for the unsteady response, and the other for the steady convergence. Both are weighted by means of a weight parameter, γ, on the range $0 \leq \gamma \leq 1$, which is to be chosen arbitrarily and in the present study is shown for its two extreme case, $\gamma = 0$ (fully steady approximation) and $\gamma = 1$ (fully unsteady modelling).

The model makes use of a convolution function for the unsteady response, and a simple multiplication for the steady-state one. The model is seen to show accurate results for short times (below the point of maximum flap-deflection speed) for $\gamma = 0$, and also for longer times for $\gamma = 1$.

It is to be noted that the model has been only used to predict the lift coefficient, and that it is left as a future task to create a similar model for the drag.

5.2 Future research

The first of the remaining tasks associated to this study is to include the effect of thickness. For the present analysis, only flat plates (with no thickness associated to them) have been taken into account. Adding thickness to the airfoil allows to use, for instance, NACA airfoils on the analysis. NACA airfoils show promising results in terms of $|\frac{C_l}{C_d}|_{max}$ for the ultra-low Reynolds number regime (as stated in Appendix B), and this way they could be included into the analysis.

Adding the effect thickness would also allow to study how the amplitude and speed effects are affected by it, and also how the model varies when it is included into the problem. This way, it may be possible, for instance, to select the best possible flap deflection for a given manoeuvre for an already-existing NACA airfoil. Camber is another parameter to be added to the profile, and whose effect study is left as a future task.

Another remaining task is to improve the presented model for the lift coefficient, seeking for more accurate results, and also to be able to automatically tune the weight parameter, γ, depending upon the case whose force evolution we would like to predict.

Besides, it is left as a future task to develop a model similar for the drag coefficient. This present several challenges, as features such as separation and turbulence has a great influence on the drag force, as well as the changes in airfoil shape due to flap deflection which modify the value of the form drag.

Finally, it is proposed to have not only a single moving piece on the airfoil (such as the flap), but also another one on it. This could be a trailing-edge tab to be placed on the airfoil flap. The purpose of this tab is to control, not the aerodynamic forces on the airfoil, but the moment produced on the flap hinge. It may happen at some stages that the force needed to either deflect the flap or

maintain it at some certain angle requires a too high moment on the flap hinge. This may be unaffordable for some small aeroplanes or MAVs. Therefore, adding a tab on the flap helps reducing the hinge moment by varying its angle of deflection, and ensures that it stays within some fixed range.

This would mean a further step into building small aircraft which are to be as most efficient as possible.

A Project budget

The project budget is estimated in this section. The main items are detailed below.

- **Computational time.** This refers to the HPC cluster which has been used for the computations. An estimation based on the Spanish CESGA center has been made, and the hour of computing has been priced to €0.2 per hour and processor. It has been estimated than approximately 1000 hours of computation have been needed, at a mean of 30 processors. This adds up to a total of €6000.

- **MATLAB license.** MATLAB has been used for post-processing. An academic license for academic purposes is priced at €500.

- **Intel compiler for Fortran.** An Intel compiler (IFORT) has been used for the Fortran code. Its cost is €999.

- **Software license.** The software in use has been a CFD code developed at the University Department [13]. However, it is necessary to assess its cost of use. In order to do this, the cost of a license for an equivalent software is to be added. The software chosen has been ANSYS Fluent, whose license has a cost of €6000 for academic and research purposes.

- **Base computer.** In order to make use of the software and to be able to do the present project, a computer has been needed. It has been an Intel-i5, TOSHIBA computer, with MICROSOFT Windows installed on it, plus a remote-interface terminal to use a Linux shell. Its price is €675.

- **Hours of work.** The price per work hour has been estimated with the price of an engineer with low experience for a research project. It has been estimated at €25 per hour of work. Around 1000 hours of work have been needed for the present project, leading to a price of €25000.

Therefore, the total cost of the project is shown in Table 5.

Subject	Price (€)
HPC time	6000
MATLAB license	500
Intel compiler	999
Software license	6000
Computer	675
Work hours	25000
Total cost	39174

Table 5: Project budget estimation.

B Airfoil analysis at ultra-low Reynolds number

Although human-made flying machines follow an increasing trend in the Reynolds number values, flying animals lay in the low-Reynolds-number regime, as stated in Section 1.1.

Micro air-vehicles (MAVs) are devices designed to fly in these natural, low-Reynolds-number area, and their study has been object of several researches [19–21]. In particular, one may want to produce MAVs with the highest possible aerodynamic efficiency, and the present study focuses on tuning the MAV airfoil for this purpose.

Potential methods will be used, implemented from XFoil-based software XFLR5. The results are to be compared to that obtained in [19] and [21], trying to assess how the different airfoil parameters affect its performance in this Reynolds-number range, and how critical they are. The Reynolds number for the simulations will range from $\mathrm{Re} = 10^3$ to $\mathrm{Re} = 5 \times 10^3$.

B.1 Airfoil shape. Bibliographic study

From [19] and [21], we get an idea of what the trends should be for a good airfoil operating in an ultra-low-Reynolds-number regime. In [19], a computational Navier-Stokes-equation solver is used to analyse the flow around airfoils for $\mathrm{Re} < 10,000$. In [21], the results are experimental, and they are obtained from a water tunnel with $\mathrm{Re} = 4 \times 10^3$.

These are to be compared to the results obtained from XFLR5, and are summarized below (this part of the study has been carried out only for NACA airfoils; other airfoil shapes will be analysed in Section B.2).

It is important to note that [21] analyses airfoil performance in terms of maximum aerodynamic efficiency, $|\frac{C_l}{C_d}|_{max}$. For this reason, the present study will also make use of the same figure of merit in seek of the best low-Reynolds-number airfoil.

B.1.1 Thickness

It is important to note that *thickness is the most critical parameter* in terms of airfoil aerodynamic efficiency.

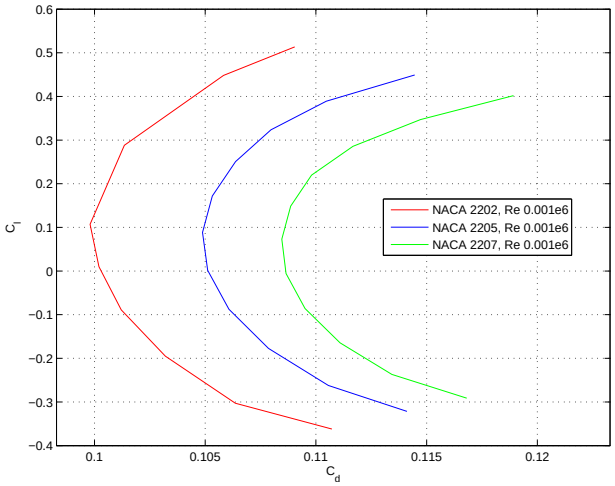

Figure 28: Thickness comparison (C_l vs C_d).

By comparing several airfoils whose only differentiating parameter is the thickness, the *thinnest* one will always have the best ratio $|\frac{C_l}{C_d}|_{max}$. This is shown in Figure 28, in which three NACA airfoils of several values of thickness are plotted.

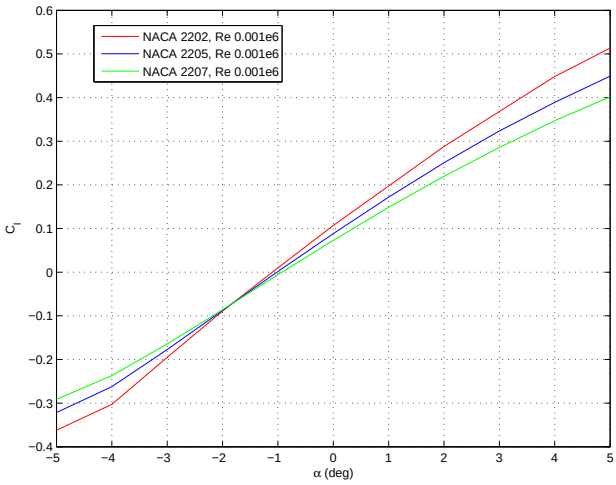

Figure 29: Thickness comparison (C_l vs α, in deg.).

A thin airfoil has a greater lift-curve slope, and is able to reach higher values of lift; this is seen in Figure 29. It also produces less drag for a given value of the angle of attack, α, as it can be noted from Figure 30. The present results match those given in [19] and [21].

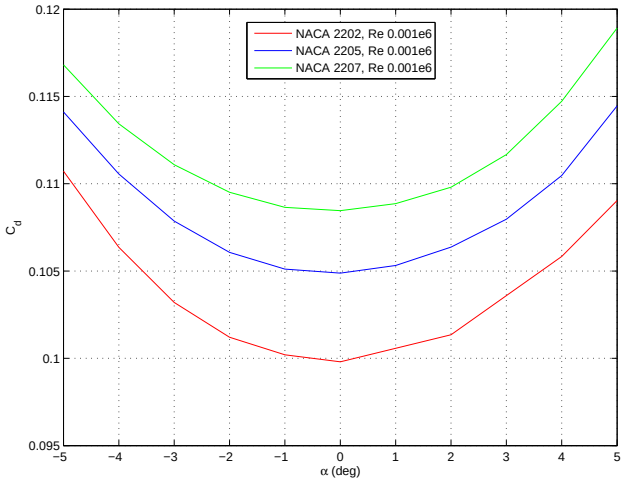

Figure 30: Thickness comparison (C_d vs α, in deg.).

B.1.2 Camber

As it is said in [21], a maximum camber of around 5% is the best one in terms of $|\frac{C_l}{C_d}|_{max}$.

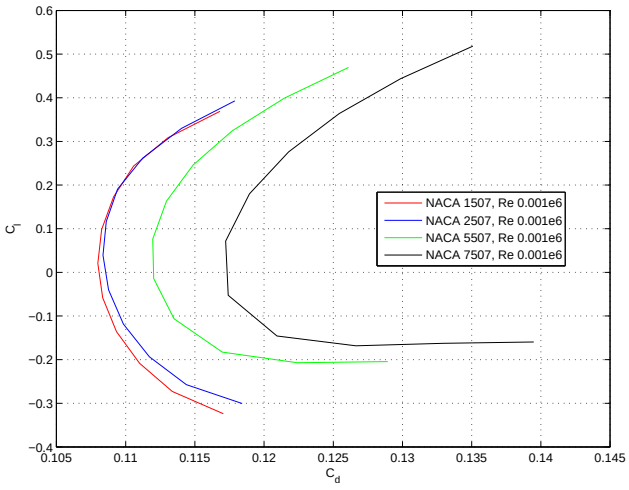

Figure 31: Camber comparison (C_l vs C_d).

The effect of the maximum camber is to increase the drag for a given value of the lift (Figure 31), and also to increase the drag as a function of α (Figure 32). However, it also increases the lift coefficient for a given α, as well as the maximum value of C_l that the airfoil is able to generate (See Figure 33).

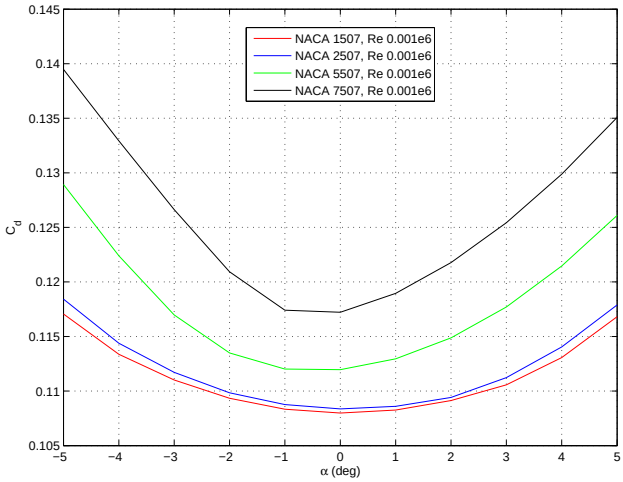

Figure 32: Camber comparison (C_d vs α, in deg.).

This means that, indeed, there is an optimum value of the maximum camber. This is found to be of 5%, as predicted by [21].

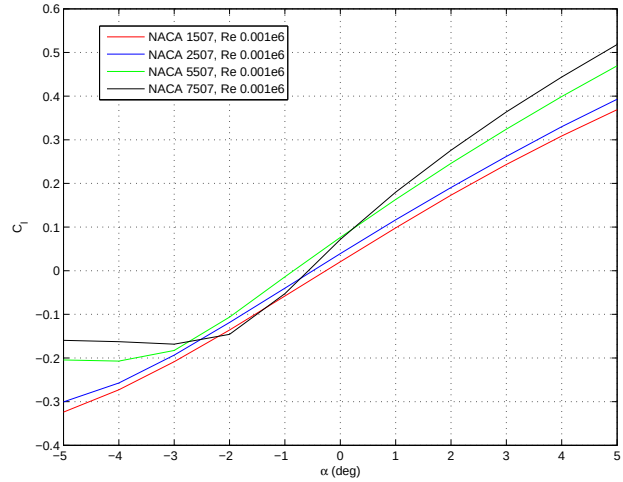

Figure 33: Camber comparison (C_l vs α, in deg.).

B.1.3 Position of maximum camber

As it is stated in [21], the further back the point of maximum camber is located, the more the drag produced for a given value of lift in the polar (see Figure 34), as well as the drag as a function of α (see Figure 35).

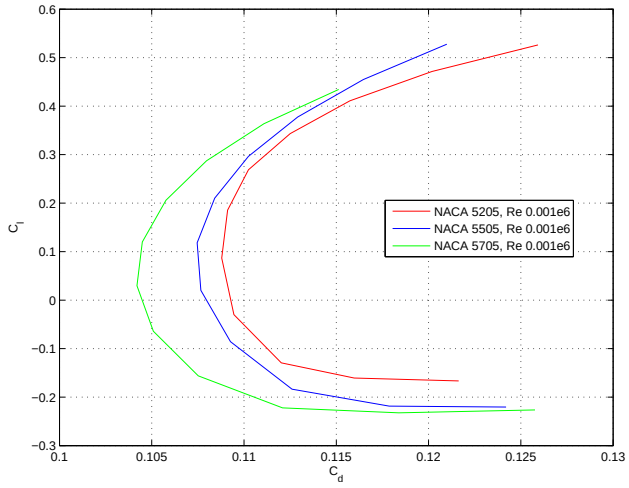

Figure 34: Comparison for the maximum-camber position (C_l vs C_d).

An aft position of maximum camber also increases the maximum value of C_l that the airfoil is able to produce (shown in Figure 36). However, the C_l is reduced for a given angle of attack due to the negative angle of attack that an aft camber induces.

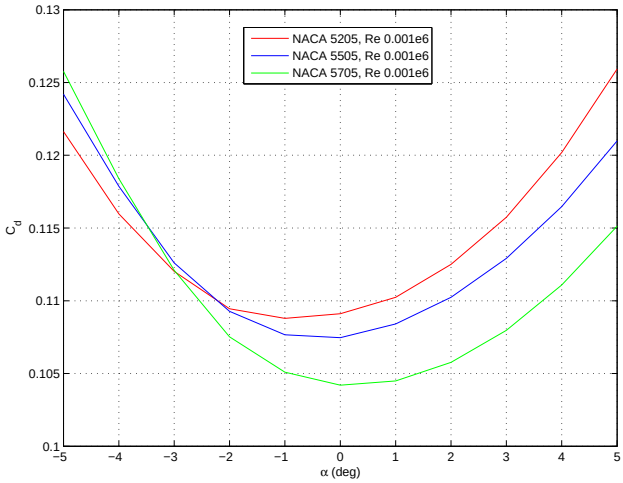

Figure 35: Comparison for the maximum-camber position (C_d vs α, in deg.).

Within the range $-5^o < \alpha < 5^o$ (as it is explained in the Section B.5), the results extracted from XFLR5 are consistent with those given in [21] (as it can be seen from Figure 34, 35 and 36), which also state that a camber position of 25% aft the leading edge gives the best possible compromise in terms of $|\frac{C_l}{C_d}|_{max}$.

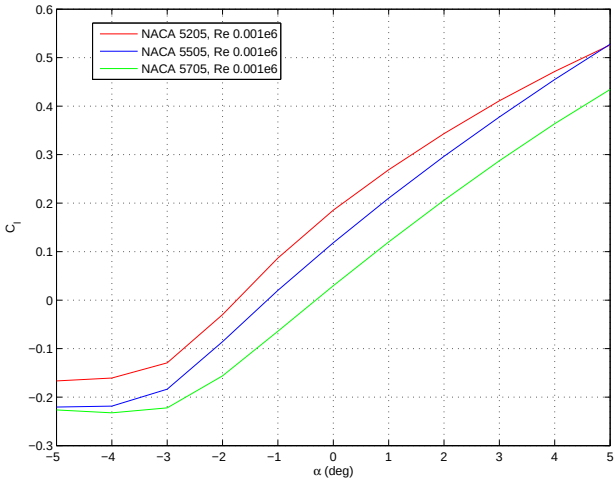

Figure 36: Comparison for the maximum-camber position (C_l vs α, in deg.).

B.2 Analysis of plates

In [21], not only NACA airfoils are studied. Instead, plates (both flat and slightly cambered) are also analysed.

The software in use, XFLR5, is only able to deal with sharp edges in the airfoil trailing edge. For the rest of the profile, a continuous shape derivative is required for the analysis to be carried out. Therefore, in principle it is not possible to study a simple plate using only XFLR5.

However, a special procedure has been carried out in order to approximate an airfoil to a plate as much as possible. For this, the leading edge of the plate has been rounded so as to eliminate the forward wall, and the leading edge is made sharp by selecting a certain value for its closing angle, Γ. Nevertheless, this is not enough to have a smooth variation of the profile shape; therefore, the profile is closed by two parabolic lines intersecting at the trailing edge (corresponding to the same value of Γ that would exist without these parabolas), as shown in Figure 37.

In principle, the value of the trailing-edge angle Γ can be arbitrarily chosen, as long as $\Gamma < 90^o$. For this study, it has been selected to be the fixed value $\Gamma = 10^o$.

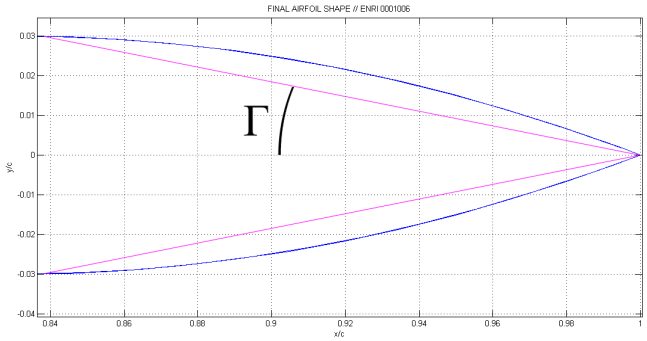

Figure 37: Trailing-edge angle and parabolic approximation.

This leads to the possibility of using a new airfoil nomenclature, *ENRI*, instead of the common NACA family. These airfoils are generated by choosing:

- Value of maximum camber in percentage of the chord (first two digits).
- Value of the position of the maximum camber in tenths of the chord, from the leading edge (next digit).

- Value of the trailing edge angle, in degrees (next two digits).
- Maximum thickness in percentage of the chord (last two digits).

An example is shown in Figure 38, where an ENRI 0001006 is shown. As it can be seen from Figure 38, the profile seems to be a flat plate except for both the leading and trailing edges.

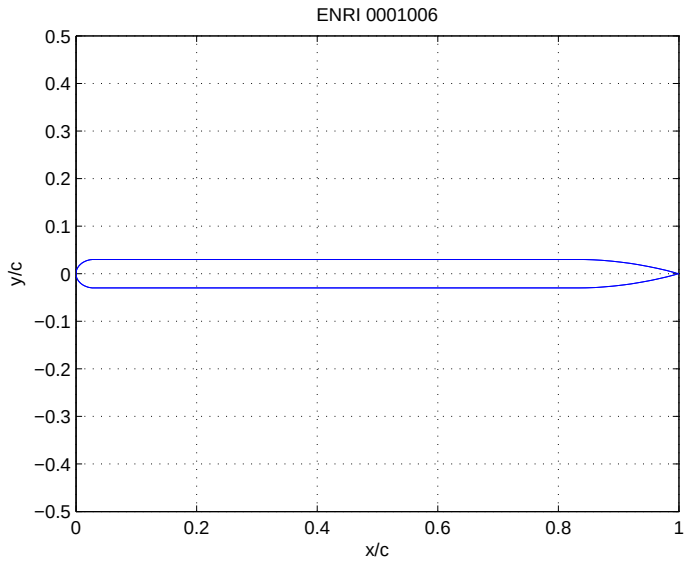

Figure 38: Example of an ENRI 0001006.

So now the next step is to assess the performance of an ENRI airfoil by comparing it to that of a flat plate, as studied in [21]. These results are plotted in Figure 39 and Figure 40.

In Figure 39, the lift coefficient as a function of the angle of attack is shown for both the flat plate (given in [21]) and its corresponding ENRI airfoil (computed using XFLR5). As it can be seen, the performance of the ENRI airfoil in terms of lift matches that of the flat plate as long as $|\alpha| < 2 - 3^o$.

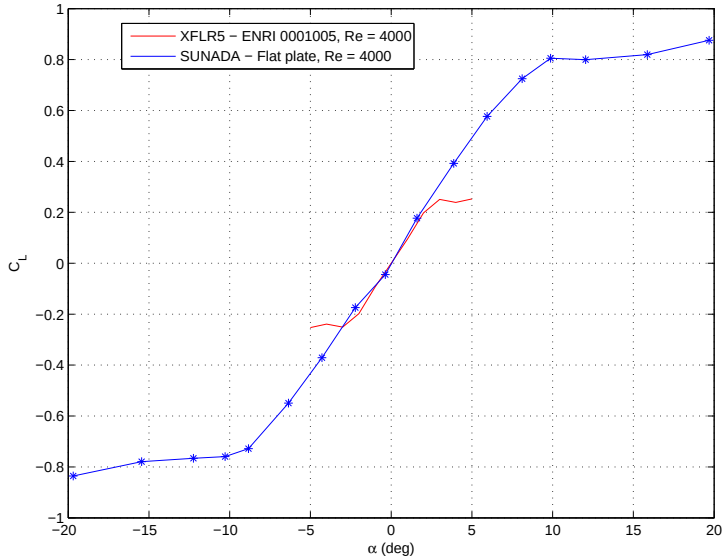

Figure 39: Comparison between a flat plate and its corresponding ENRI airfoil (C_l vs α, in deg.).

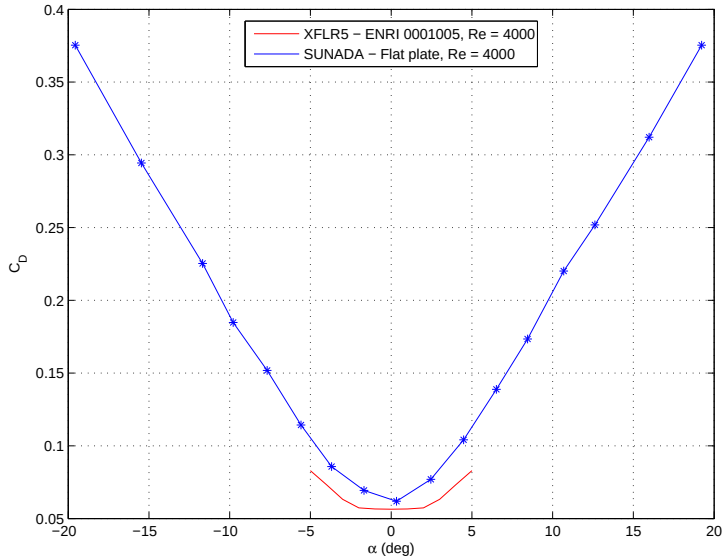

Figure 40: Comparison between a flat plate and its corresponding ENRI airfoil (C_d vs α, in deg.).

In terms of drag (see Figure 40), the difference is higher, and the performance of the ENRI airfoil is seen to be better (less drag generation) than that of a simple

flat plate.

However, the difference is of the order of 10%, which is considered to be negligible, so that it is to be assumed that the deductions in [21] for a flat plate are comparable to an ENRI airfoil of the same characteristics[1].

[1]There is also a difference associated with the error made by XFLR5 itself, as discussed in Section B.5

B.3 NACA and ENRI comparison

After the way to analyse plates has been defined, it is now time to check whether plates may be better than NACA airfoils in terms of $|\frac{C_l}{C_d}|_{max}$ or not.

In order to assess the performance of the ENRI airfoil, compared to an NACA, an illustrative example for each of them has been studied (an NACA 5206 and its equivalent ENRI 0521006), and their characteristics in terms of lift and drag has been consequently compared. According to [21], the NACA airfoil is better than a flat plate, and so we expect the NACA airfoils to be better than their corresponding ENRI airfoils.

Figure 41 shows the C_l as a function of α, for both the NACA and its equivalent ENRI. Although it is true that the NACA performance is better in general, the difference is of the order of a 3% at $\alpha = 3$ degrees. This is considered to be negligible, so that the ENRI airfoil can in principle be used as a good sample for a first approximation.

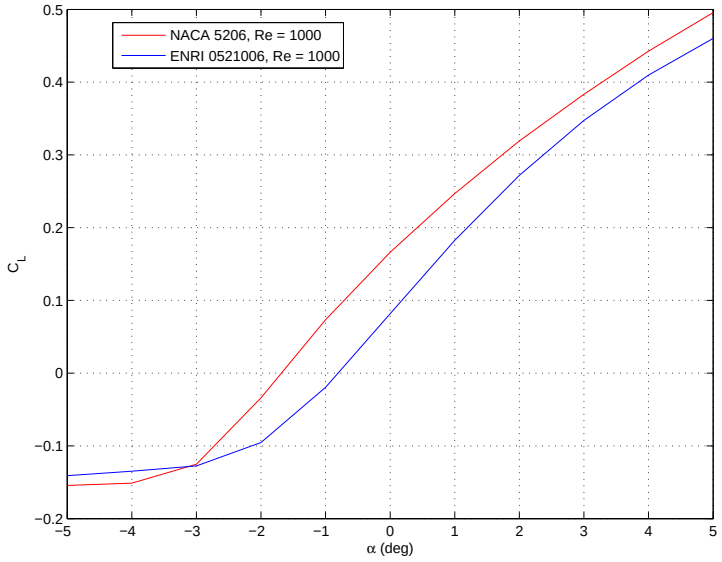

Figure 41: NACA and ENRI comparison (C_l vs α, in deg.).

Something similar happens for the drag coefficient (shown in Figure 42): as expected, the drag produced by an NACA is in general smaller. However, the difference is again reasonably small (of the order of 5% for $\alpha = 3$ degrees) to be able to select the ENRI airfoil instead of the NACA in some specific situations.

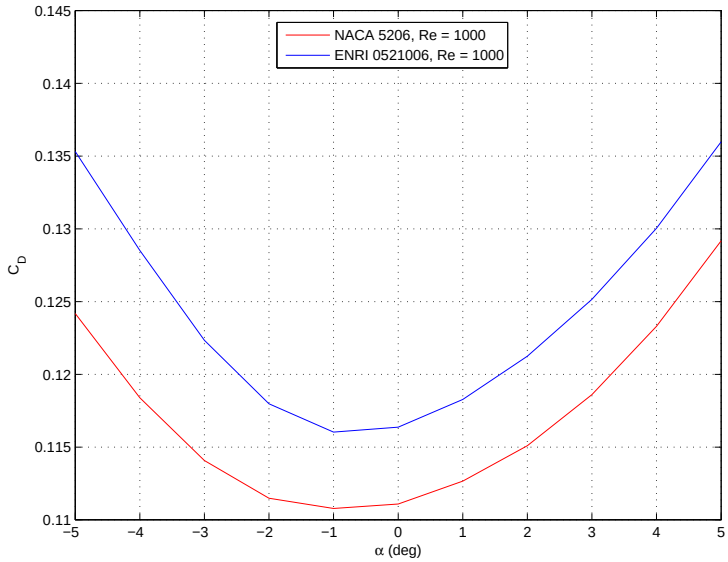

Figure 42: NACA and ENRI comparison (C_d vs α, in deg.).

B.4 First conclusions

As a result for a first approximation using XFoil-based software and the results given by [19] and [21], the following conclusions are reached for the characteristics of the airfoil:

- The thickness should be as small as possible. Because of mechanical and manufacturing constraints, an airfoil thickness of around 5% is proposed.
- The value of the maximum camber which gives the best performance in terms of $|\frac{C_l}{C_d}|_{max}$ corresponds to a 5% of the chord length.
- The location of this maximum camber should be 25% of the chord length from the leading edge.
- An NACA airfoil presents better performance in terms of $|\frac{C_l}{C_d}|_{max}$ than a plate of the same characteristics (being the plate analysed as an ENRI airfoil). However, the difference is negligible so that a flat plate can be used in some situations as a first approximation to the problem.

This means that a good approximation to the best airfoil for $1000 < \mathrm{Re} < 5000$ is an NACA 5305. This is illustrated in Figure 43, where this airfoil, *(a)*, is compared to some others, in *(b)*.

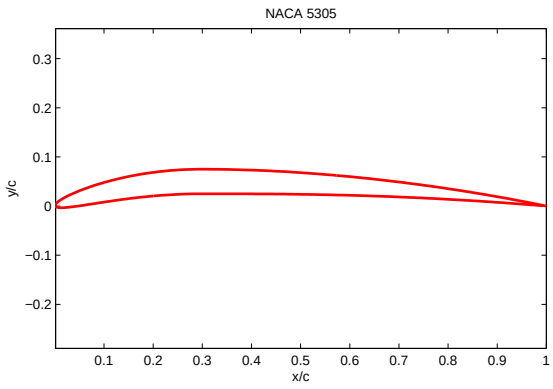

(a)

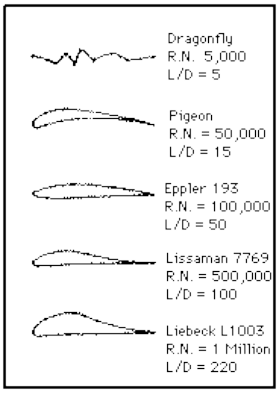

(b)

Figure 43: The proposed airfoil as compared to some noticeable examples[2].

It is interesting to note the similarity of the NACA 5305 and the pigeon airfoil, for instance. The first section corresponds to a dragonfly, and does not need to be smooth at all. This is because for Reynolds numbers smaller than some critical value of around $\mathrm{Re}_c = 3 \times 10^3$, roughness does not influence the friction factor[3]. Besides, corrugation improves wing rigidity, which is also good for this animal.

The other airfoils in Figure 43 are early-developments; specifically, the Lissaman 7769 was intended to serve for human-powered aircraft [20].

[2]Figure 43.b extracted from [20].

[3]As it is illustrated in the so-called Moody diagram.

B.5 Note on the validity of XFLR5

XFLR5 is an XFoil-based software, which makes use of potential-flow analysis in a 2-dimensional way. This would in principle imply that transition to turbulence, flow separation and boundary-layer effect are not taken into account in the solution.

Nevertheless, XFLR5 presents its own model to simulate these effects. However, this is not enough to properly reach a solution for the flow in all cases, due to several reasons:

- First of all, turbulence is a fully-3-dimensional problem, which cannot, in principle, be solved as a 2-dimensional issue. This implies that, once the flow is separated from the body, the solution provided by XFLR5 is no longer valid.
- Besides, the point of separation of the flow is not properly predicted, due to the simplicity of the model. Separation is quite a complex issue, which is affected by many parameters, and it is not possible to predict it properly.
- Finally, the boundary layer is fully influenced by turbulence and separation, which leads to a solution not properly defined for it.

These facts make clear that it is important to be careful while working with this XFoil-based tool, because the obtained results may not be correct at all.

Based on the angle of attack, it has been assessed that XFLR5 is able to present a good solution for the flow as long as $-5^o < \alpha < 5^o$. For higher values of $|\alpha|$, both transition to turbulence and flow separation effects take place, which make the XFoil-based solution no longer a valid one.

In order to fully validate the method, the results given for a specific airfoil have been compared to that known to be correct for that specific profile.

Specifically, it has been validated by studying the behaviour of an NACA 0006. The results extracted from the program are compared to those obtained by [21].

The result for the lift as a function of the angle of attack is shown in Figure 44, while that for the drag is given in Figure 45.

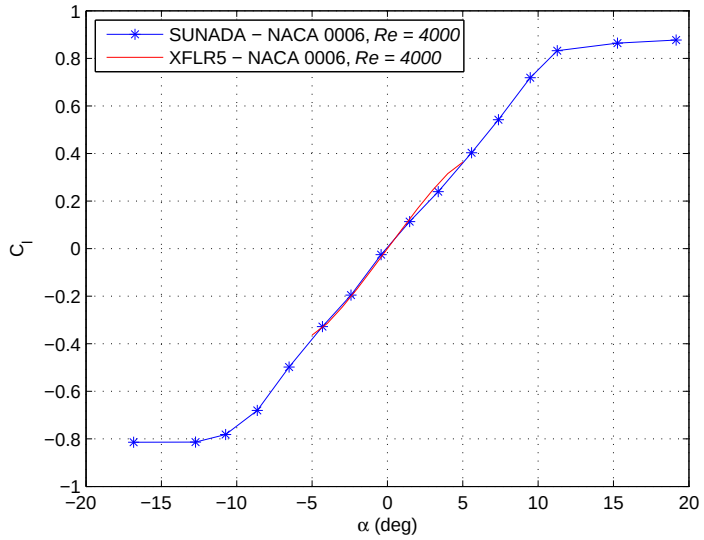

Figure 44: Validation of the XFLR5 analysis (C_l vs α, in deg.).

As it can be seen, the results for the lift are accurate enough to take the XFLR5 analysis as a good method for a first approximation.

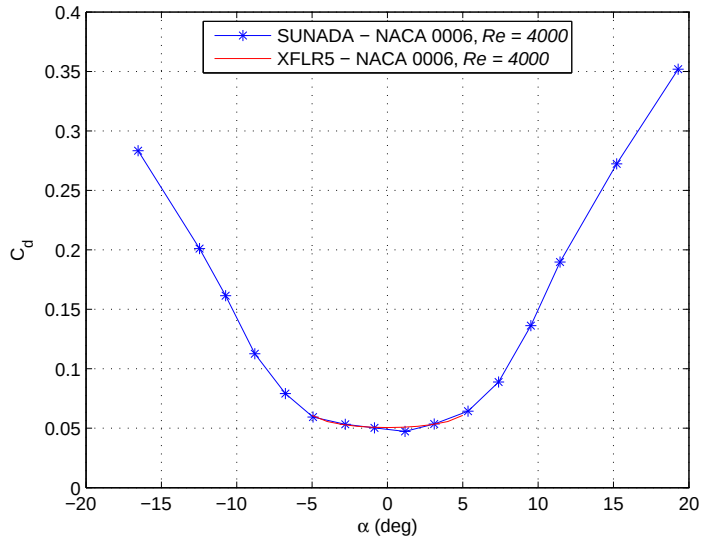

Figure 45: Validation of the XFLR5 analysis (C_d vs α, in deg.).

In the case of the drag, the difference is also small. It is important to note that

the difference in drag is usually higher than that in lift. This is because the drag coefficient is defined to be

$$C_D = C_{D_0} + k{C_L}^2, \tag{14}$$

for a wing, where $k = \frac{1}{\pi e AR}$, being e the Oswald coefficient and AR the wing aspect ratio.

The parabolic term (or *induced drag*), proportional to C_L^2, is very accurately predicted by XFLR5 (because, as shown in Figure 44, the lift coefficient is well predicted for the airfoil). However, in here, the small error that the lift may present is squared, so it becomes very critical. Besides, the other term, C_{D_0} (or *parasitic drag*), is related to skin friction and form drag, which are fully influenced by turbulent effects. This is why this value may differ slightly from the one given in [21].

Nevertheless, the prediction is still god enough to say that XFLR5 is a good measure of the flow properties and dependences on a first approximation to the problem.

References

[1] Cross, James. "FAA being urged to tighten restrictions on drone use." KTAR News (2014), http://ktar.com/22/1732063/FAA-being-urged-to-tighten-restrictions-on-drone-use

[2] The US Federal Aviation Administration, Unmanned Aircraft Systems, http://www.faa.gov/about/initiatives/uas/

[3] Sane, Sanjay P. "The aerodynamics of insect flight." The journal of experimental biology 206, no. 23 (2003): 4191-4208

[4] Frederick, M., E. C. Kerrigan, and J. M. R. Graham. "Gust alleviation using rapidly deployed trailing-edge flaps." Journal of Wind Engineering and Industrial Aerodynamics 98.12 (2010): 712-723.

[5] Lee, T., and Y. Y. Su. "Unsteady airfoil with a harmonically deflected trailing-edge flap." Journal of Fluids and Structures 27.8 (2011): 1411-1424.

[6] Krzysiak, A., and Narkiewicz, J. "Aerodynamic loads on airfoil with trailing-edge flap pitching with different frequencies." Journal of aircraft 43.2 (2006): 407-418.

[7] Gerontakos, P., and T. Lee. "PIV study of flow around unsteady airfoil with dynamic trailing-edge flap deflection." Experiments in fluids 45.6 (2008): 955-972.

[8] Gerontakos, P. and Lee, T. "Trailing-Edge Flap Control of Dynamic Pitching Moment", AIAA Journal, Vol. 45, No. 7 (2007), pp. 1688-1694.

[9] Gerontakos, P., and Lee, T. "Active trailing-edge flap control of oscillating-wing tip vortex." AIAA journal 44.11 (2006): 2746-2754.

[10] Choi, S., and Chang, K. "Navier-Stokes computation of a rapidly deploying spoiler." Journal of aircraft 37.4 (2000): 655-661.

[11] Hariharan, N., and Leishman, J. G. "Unsteady aerodynamics of a flapped airfoil in subsonic flow by indicial concepts." Journal of Aircraft 33.5 (1996): 855-868.

[12] Uhlmann, Markus. "An immersed boundary method with direct forcing for the simulation of particulate flows". Journal of Computational Physics 209.2 (2005): 448-476.

[13] Moriche, Manuel. "Development and validation of a numerical solver for unsteady aerodynamic applications". Master Thesis, Carlos III University. (2013)

[14] Courant, Richard, Kurt Friedrichs, and Hans Lewy. "On the partial difference equations of mathematical physics." IBM journal of Research and Development 11.2 (1967): 215-234.

[15] Lax, Peter D. "Hyperbolic difference equations: A review of the Courant-Friedrichs-Lewy paper in the light of recent developments." IBM Journal of Research and Development 11.2 (1967): 235-238.

[16] Anderson Jr, John David. "Fundamentals of aerodynamics". Tata McGraw-Hill Education, 1985.

[17] Glat, lgen. "Fundamentals of modern unsteady aerodynamics". Springer, 2010.

[18] Bisplinghoff, Raymond L., Holt Ashley, and Robert L. Halfman. "Aeroelasticity". Courier Dover Publications, 2013.

[19] Kunz, P., and I. Kroo. "Analysis, design, and testing of airfoils for use at ultra-low Reynolds numbers". Proceedings of a Workshop on Fixed and Flapping Flight at Low Reynolds Numbers, Notre Dame. 2000.

[20] Lissaman, P. B. S. "Low-Reynolds-number airfoils". Annual Review of Fluid Mechanics 15.1 (1983): 223-239.

[21] Sunada, S., et al. "Comparison of wing characteristics at an ultralow Reynolds number". Journal of aircraft 39.2 (2002): 331-338.